given the severe muscular atrophy present in the AR-97Q mice (Katsuno et al., 2002). In support of this view, a previous study showed that inhibition of myostatin has little effect on muscle damage in rodent models of ALS (Holzbaur et al., 2006).

The TGF-β-Smad2/3 pathway is also known to regulate the function of glial cells. However, a great deal of debate has been waged on how glial TGF-β signaling modulates the pathogenesis of neurodegeneration. TGF-β was shown to activate astrocytes and to protect against neuron damage caused by brain injury, while the overexpression of TGF-β in astrocytes promotes brain inflammation and AD-like microvascular degeneration (Flanders et al., 1998; Wyss-Coray et al., 2000). In polyglutamine diseases, the pathogenic proteins accumulate exclusively in neurons, suggesting that neuronal involvement is the primary molecular event triggering neurodegeneration. In accordance with this hypothesis, the present study suggests that the neuronal TGF-β-Smad2/3 pathway plays a substantial role in the molecular mechanisms underlying polyglutamine-mediated neurodegeneration, given that TGF-β signaling was disturbed both in transfected cultured neuronal cells and in neurons of diseased patients and mice.

In conclusion, the present study showed that polyglutamine-dependent neuron damage in SBMA is associated with the disruption of TGF-β signaling due to transcriptional dysregulation of TβRII. Our findings further suggest that restoration of the brain TGF-β-Smad2/3 pathway might be a potential therapeutic approach to polyglutamine-induced neurodegenerative diseases.

References

Adachi H, Kumiai A, Li M, Nakagomi Y, Niwa H, Do J, Sang C, Kobayashi Y, Doyu M, Sobue G (2001) Transgenic mice with an expanded CAG repeat controlled by the human AR promoter show polyglutamine nuclear inclusions and neuronal dysfunction without neuronal cell death. Hum Mol Genet 10:1039–1048.

Adachi H, Katsuno M, Minamiyama M, Sang C, Pagoulatos G, Angelidis C, Kusakabe M, Yoshiki A, Kobayashi Y, Doyu M, Sobue G (2003) Heat shock protein 70 chaperone overexpression ameliorates phenotypes of the spinal and bulbar muscular atrophy transgenic mouse model by reducing nuclear-localized mutant androgen receptor protein. J Neurosci 23:2203–2211.

Adachi H, Katsuno M, Minamiyama M, Waza M, Sang C, Nakagomi Y, Kobayashi Y, Tanaka F, Doyu M, Inukai A, Yoshida M, Hashizume Y, Sobue G (2005) Widespread nuclear and cytoplasmic accumulation of mutant androgen receptor in SBMA patients. Brain 128:659–670.

Adachi H, Waza M, Tokui K, Katsuno M, Minamiyama M, Tanaka F, Doyu M, Sobue G (2007) CHIP overexpression reduces mutant androgen receptor protein and ameliorates phenotypes of the spinal and bulbar muscular atrophy transgenic mouse model. J Neurosci 27:5115–5126.

Andrews ZB, Zhao H, Frugier T, Meguro R, Grattan DR, Koishi K, McLennan IS (2006) Transforming growth factor beta2 haploinsufficient mice develop age-related nigrostriatal dopamine deficits. Neurobiol Dis 21:568–575.

Banno H, Katsuno M, Suzuki K, Takeuchi Y, Kawashima M, Suga N, Takamori M, Ito M, Nakamura T, Matsuo K, Yamada S, Oki Y, Adachi H, Minamiyama M, Waza M, Atsuta N, Watanabe H, Fujimoto Y, Nakashima T, Tanaka F, et al. (2009) Phase 2 trial of leuprorelin in patients with spinal and bulbar muscular atrophy. Ann Neurol 65:140–150.

Brionne TC, Tesseur I, Masliah E, Wyss-Coray T (2003) Loss of TGF-beta 1 leads to increased neuronal cell death and microgliosis in mouse brain. Neuron 40:1133–1145.

Butler R, Bates GP (2006) Histone deacetylase inhibitors as therapeutics for polyglutamine disorders. Nat Rev Neurosci 7:784–796.

Chevalier-Larsen ES, O'Brien CJ, Wang H, Jenkins SC, Holder L, Lieberman AP, Merry DE (2004) Castration restores function and neurofilament alterations of aged symptomatic males in a transgenic mouse model of spinal and bulbar muscular atrophy. J Neurosci 24:4778–4786.

Chou AH, Yeh TH, Ouyang P, Chen YL, Chen SY, Wang HL (2008) Polyglutamine-expanded ataxin-3 causes cerebellar dysfunction of SCA3 transgenic mice by inducing transcriptional dysregulation. Neurobiol Dis 31:89–101.

Colavita A, Krishna S, Zheng H, Padgett RW, Culotti JG (1998) Pioneer axon guidance by UNC-129, a C. elegans TGF-beta. Science 281:706–709.

Cui L, Jeong H, Borovecki F, Parkhurst CN, Tanese N, Krainc D (2006) Transcriptional repression of PGC-1alpha by mutant huntingtin leads to mitochondrial dysfunction and neurodegeneration. Cell 127:59–69.

Dunah AW, Jeong H, Griffin A, Kim YM, Standaert DG, Hersch SM, Mouradian MM, Young AB, Tanese N, Krainc D (2002) Sp1 and TAFII130 transcriptional activity disrupted in early Huntington's disease. Science 296:2238–2243.

Fernandes HB, Baimbridge KG, Church J, Hayden MR, Raymond LA (2007) Mitochondrial sensitivity and altered calcium handling underlie enhanced NMDA-induced apoptosis in YAC128 model of Huntington's disease. J Neurosci 27:13614–13623.

Flanders KC, Ren RF, Lippa CF (1998) Transforming growth factor-betas in neurodegenerative disease. Prog Neurobiol 54:71–85.

Gatchel JR, Zoghbi HY (2005) Diseases of unstable repeat expansion: mechanisms and common principles. Nat Rev Genet 6:743–755.

Hay DG, Sathasivam K, Tobaben S, Stahl B, Marber M, Mestril R, Mahal A, Smith DL, Woodman B, Bates GP (2004) Progressive decrease in chaperone protein levels in a mouse model of Huntington's disease and induction of stress proteins as a therapeutic approach. Hum Mol Genet 13:1389–1405.

Heupel K, Sargsyan V, Plomp JJ, Rickmann M, Varoqueaux F, Zhang W, Krieglstein K (2008) Loss of transforming growth factor-beta 2 leads to impairment of central synapse function. Neural Dev 3:25.

Hockly E, Richon VM, Woodman B, Smith DL, Zhou X, Rosa E, Sathasivam K, Ghazi-Noori S, Mahal A, Lowden PA, Steffan JS, Marsh JL, Thompson LM, Lewis CM, Marks PA, Bates GP (2003) Suberoylanilide hydroxamic acid, a histone deacetylase inhibitor, ameliorates motor deficits in a mouse model of Huntington's disease. Proc Natl Acad Sci U S A 100:2041–2046.

Holzbaur EL, Howland DS, Weber N, Wallace K, She Y, Kwak S, Tchistiakova LA, Murphy E, Hinson J, Karim R, Tan XY, Kelley P, McGill KC, Williams G, Hobbs C, Doherty P, Zaleska MM, Pangalos MN, Walsh FS (2006) Myostatin inhibition slows muscle atrophy in rodent models of amyotrophic lateral sclerosis. Neurobiol Dis 23:697–707.

Jin S, Scotto KW (1998) Transcriptional regulation of the MDR1 gene by histone acetyltransferase and deacetylase is mediated by NF-Y. Mol Cell Biol 18:4377–4384.

Katsuno M, Adachi H, Kume A, Li M, Nakagomi Y, Niwa H, Sang C, Kobayashi Y, Doyu M, Sobue G (2002) Testosterone reduction prevents phenotypic expression in a transgenic mouse model of spinal and bulbar muscular atrophy. Neuron 35:843–854.

Katsuno M, Adachi H, Doyu M, Minamiyama M, Sang C, Kobayashi Y, Inukai A, Sobue G (2003) Leuprorelin rescues polyglutamine-dependent phenotypes in a transgenic mouse model of spinal and bulbar muscular atrophy. Nat Med 9:768–773.

Katsuno M, Sang C, Adachi H, Minamiyama M, Waza M, Tanaka F, Doyu M, Sobue G (2005) Pharmacological induction of heat-shock proteins alleviates polyglutamine-mediated motor neuron disease. Proc Natl Acad Sci U S A 102:16801–16806.

Katsuno M, Adachi H, Waza M, Banno H, Suzuki K, Tanaka F, Doyu M, Sobue G (2006a) Pathogenesis, animal models and therapeutics in spinal and bulbar muscular atrophy (SBMA). Exp Neurol 200:8–18.

Katsuno M, Adachi H, Minamiyama M, Waza M, Tokui K, Banno H, Suzuki K, Onoda Y, Tanaka F, Doyu M, Sobue G (2006b) Reversible disruption of dynactin 1-mediated retrograde axonal transport in polyglutamine-induced motor neuron degeneration. J Neurosci 26:12106–12117.

La Spada AR, Wilson EM, Lubahn DB, Harding AE, Fischbeck KH (1991) Androgen receptor gene mutations in X-linked spinal and bulbar muscular atrophy. Nature 352:77–79.

Li M, Miwa S, Kobayashi Y, Merry DE, Yamamoto M, Tanaka F, Doyu M, Hashizume Y, Fischbeck KH, Sobue G (1998) Nuclear inclusions of the androgen receptor protein in spinal and bulbar muscular atrophy. Ann Neurol 44:249–254.

Lin X, Antalffy B, Kang D, Orr HT, Zoghbi HY (2000) Polyglutamine expansion down-regulates specific neuronal genes before pathologic changes in SCA1. Nat Neurosci 3:157–163.

Luthi-Carter R, Strand A, Peters NL, Solano SM, Hollingsworth ZR, Menon AS, Frey AS, Spektor BS, Penney EB, Schilling G, Ross CA, Borchelt DR,

Tapscott SJ, Young AB, Cha JH, Olson JM (2000) Decreased expression of striatal signaling genes in a mouse model of Huntington's disease. Hum Mol Genet 9:1259–1271.

McPherron AC, Lawler AM, Lee SJ (1997) Regulation of skeletal muscle mass in mice by a new TGF-beta superfamily member. Nature 387:83–90.

Minamiyama M, Katsuno M, Adachi H, Waza M, Sang C, Kobayashi Y, Tanaka F, Doyu M, Inukai A, Sobue G (2004) Sodium butyrate ameliorates phenotypic expression in a transgenic mouse model of spinal and bulbar muscular atrophy. Hum Mol Genet 13:1183–1192.

Niwa H, Yamamura K, Miyazaki J (1991) Efficient selection for high-expression transfectants with a novel eukaryotic vector. Gene 108:193–199.

Nucifora FC Jr, Sasaki M, Peters MF, Huang H, Cooper JK, Yamada M, Takahashi H, Tsuji S, Troncoso J, Dawson VL, Dawson TM, Ross CA (2001) Interference by huntingtin and atrophin-1 with cbp-mediated transcription leading to cellular toxicity. Science 291:2423–2428.

Palhan VB, Chen S, Peng GH, Tjernberg A, Gamper AM, Fan Y, Chait BT, La Spada AR, Roeder RG (2005) Polyglutamine-expanded ataxin-7 inhibits STAGA histone acetyltransferase activity to produce retinal degeneration. Proc Natl Acad Sci U S A 102:8472–8477.

Park SH, Lee SR, Kim BC, Cho EA, Patel SP, Kang HB, Sausville EA, Nakanishi O, Trepel JB, Lee BI, Kim SJ (2002) Transcriptional regulation of the transforming growth factor beta type II receptor gene by histone acetyltransferase and deacetylase is mediated by NF-Y in human breast cancer cells. J Biol Chem 277:5168–5174.

Peart MJ, Smyth GK, van Laar RK, Bowtell DD, Richon VM, Marks PA, Holloway AJ, Johnstone RW (2005) Identification and functional significance of genes regulated by structurally different histone deacetylase inhibitors. Proc Natl Acad Sci U S A 102:3697–3702.

Ranganathan S, Harmison GG, Meyertholen K, Pennuto M, Burnett BG, Fischbeck KH (2009) Mitochondrial abnormalities in spinal and bulbar muscular atrophy. Hum Mol Genet 18:27–42.

Riley BE, Orr HT (2006) Polyglutamine neurodegenerative diseases and regulation of transcription: assembling the puzzle. Genes Dev 20:2183–2192.

Sadri-Vakili G, Bouzou B, Benn CL, Kim MO, Chawla P, Overland RP, Glajch KE, Xia E, Qiu Z, Hersch SM, Clark TW, Yohrling GJ, Cha JH (2007) Histones associated with downregulated genes are hypo-acetylated in Huntington's disease models. Hum Mol Genet 16:1293–1306.

Sanyal S, Kim SM, Ramaswami M (2004) Retrograde regulation in the CNS; neuron-specific interpretations of TGF-beta signaling. Neuron 41:845–848.

Shi Y, Massague J (2003) Mechanisms of TGF-beta signaling from cell membrane to the nucleus. Cell 113:685–700.

Steffan JS, Bodai L, Pallos J, Poelman M, McCampbell A, Apostol BL, Kazantsev A, Schmidt E, Zhu YZ, Greenwald M, Kurokawa R, Housman DE, Jackson GR, Marsh JL, Thompson LM (2001) Histone deacetylase inhibitors arrest polyglutamine-dependent neurodegeneration in Drosophila. Nature 413:739–743.

Takeyama K, Ito S, Yamamoto A, Tanimoto H, Furutani T, Kanuka H, Miura M, Tabata T, Kato S (2002) Androgen-dependent neurodegeneration by polyglutamine-expanded human androgen receptor in Drosophila. Neuron 35:855–864.

Tesseur I, Zou K, Esposito L, Bard F, Berber E, Can JV, Lin AH, Crews L, Tremblay P, Mathews P, Mucke L, Masliah E, Wyss-Coray T (2006) Deficiency in neuronal TGF-beta signaling promotes neurodegeneration and Alzheimer's pathology. J Clin Invest 116:3060–3069.

Tokui K, Adachi H, Waza M, Katsuno M, Minamiyama M, Doi H, Tanaka K, Hamazaki J, Murata S, Tanaka F, Sobue G (2009) 17-DMAG ameliorates polyglutamine-mediated motor neuron degeneration through well-preserved proteasome function in an SBMA model mouse. Hum Mol Genet 18:898–910.

Vivien D, Ali C (2006) Transforming growth factor-beta signalling in brain disorders. Cytokine Growth Factor Rev 17:121–128.

Waza M, Adachi H, Katsuno M, Minamiyama M, Sang C, Tanaka F, Inukai A, Doyu M, Sobue G (2005) 17-AAG, an Hsp90 inhibitor, ameliorates polyglutamine-mediated motor neuron degeneration. Nat Med 11:1088–1095.

Wyss-Coray T, Lin C, Sanan DA, Mucke L, Masliah E (2000) Chronic overproduction of transforming growth factor-beta1 by astrocytes promotes Alzheimer's disease-like microvascular degeneration in transgenic mice. Am J Pathol 156:139–150.

Yamanaka T, Miyazaki H, Oyama F, Kurosawa M, Washizu C, Doi H, Nukina N (2008) Mutant Huntingtin reduces HSP70 expression through the sequestration of NF-Y transcription factor. EMBO J 27:827–839.

Ying M, Xu R, Wu X, Zhu H, Zhuang Y, Han M, Xu T (2006) Sodium butyrate ameliorates histone hypoacetylation and neurodegenerative phenotypes in a mouse model for DRPLA. J Biol Chem 281:12580–12586.

Zheng X, Zugates CT, Lu Z, Shi L, Bai JM, Lee T (2006) Baboon/dSmad2 TGF-beta signaling is required during late larval stage for development of adult-specific neurons. EMBO J 25:615–627.

Zhu Y, Yang GY, Ahlemeyer B, Pang L, Che XM, Culmsee C, Klumpp S, Krieglstein J (2002) Transforming growth factor-beta 1 increases bad phosphorylation and protects neurons against damage. J Neurosci 22:3898–3909.

Neuron
Article

New Neurons Clear the Path of Astrocytic Processes for Their Rapid Migration in the Adult Brain

Naoko Kaneko,[1] Oscar Marín,[2] Masato Koike,[3] Yuki Hirota,[1] Yasuo Uchiyama,[3] Jane Y. Wu,[4] Qiang Lu,[5] Marc Tessier-Lavigne,[6] Arturo Alvarez-Buylla,[7] Hideyuki Okano,[8] John L.R. Rubenstein,[9] and Kazunobu Sawamoto[1,*]
[1]Department of Developmental and Regenerative Biology, Institute of Molecular Medicine, Nagoya City University Graduate School of Medical Sciences, Nagoya, Aichi, 467-8601, Japan
[2]Instituto de Neurociencias, Consejo Superior de Investigaciones Científicas and Universidad Miguel Hernández, Sant Joan d'Alcant 03550, Alicante, Spain
[3]Department of Cell Biology and Neuroscience, Juntendo University Graduate School of Medicine, Bunkyo-ku, Tokyo, 113-0033, Japan
[4]Department of Neurology and Center for Genetic Medicine, Northwestern University Feinberg School of Medicine, Chicago IL, 60611, USA
[5]Division of Neuroscience, Beckman Research Institute of the City of Hope, Duarte, CA 81657, USA
[6]Genentech, South San Francisco, CA 94080, USA
[7]Department of Neurological Surgery and Institute for Regeneration Medicine, University of California at San Francisco, San Francisco, CA 94143, USA
[8]Department of Physiology, Keio University School of Medicine, Shinjyuku-ku, Tokyo, 160-8582, Japan
[9]Nina Ireland Laboratory of Developmental Neurobiology, Center for Neurobiology and Psychiatry, University of California at San Francisco, San Francisco, CA 94143, USA
*Correspondence: sawamoto@med.nagoya-cu.ac.jp
DOI 10.1016/j.neuron.2010.06.018

SUMMARY

In the long-range neuronal migration of adult mammals, young neurons travel from the subventricular zone to the olfactory bulb, a long journey (millimeters to centimeters, depending on the species). How can these neurons migrate through the dense meshwork of neuronal and glial processes of the adult brain parenchyma? Previous studies indicate that young neurons achieve this by migrating in chains through astrocytic tunnels. Here, we report that young migrating neurons actively control the formation and maintenance of their own migration route. New neurons secrete the diffusible protein Slit1, whose receptor, Robo, is expressed on astrocytes. We show that the Slit-Robo pathway is required for morphologic and organizational changes in astrocytes that result in the formation and maintenance of the astrocytic tunnels. Through this neuron-glia interaction, the new neurons regulate the formation of the astrocytic meshwork that is needed to enable their rapid and directional migration in adult brain.

INTRODUCTION

In the developing brain, immature neurons are produced in specific brain regions and migrate to their final destinations, where they assume their mature neuronal functions. Previous studies have established that this process is controlled by various extracellular signals in the neurons' surroundings that are mediated by transmembrane receptors expressed on the migrating neurons (**Hatten, 2002**; **Marín and Rubenstein, 2003**). However, little is known about the role migrating neurons may play in the formation and maintenance of their own migration route.

In the adult brain, new neurons are continuously generated in the subventricular zone (SVZ) at the lateral walls of the lateral ventricles, and they migrate into the olfactory bulb (OB), located at the anterior tip of the telencephalon. Throughout life, newly generated immature neurons migrate through the rostral migratory stream (RMS), the pathway leading to the OB (**Doetsch and Alvarez-Buylla, 1996**; **Jankovski and Sotelo, 1996**; **Lois and Alvarez-Buylla, 1994**; **Petreanu and Alvarez-Buylla, 2002**). How can these neurons migrate through the dense meshwork of neuronal and glial processes of the adult brain parenchyma? During migration, the neurons in the RMS are unipolar or bipolar, with extended leading and trailing processes, and they form elongated cell aggregates called "chains," within which they move over and past one another. The chains of neurons move inside tunnels formed by astrocytic processes, referred to as "glial tubes" (**Jankovski and Sotelo, 1996**; **Kaneko and Sawamoto, 2009**; **Lois et al., 1996**; **Okano and Sawamoto, 2008**). In several lines of mutant mice, aberrant astrocytic-tube formation is accompanied by a disruption in new-neuron chain migration (**Anton et al., 2004**; **Belvindrah et al., 2007**; **Chazal et al., 2000**; **Ghashghaei et al., 2006**), suggesting that efficient neuronal migration in the adult brain depends on interactions between the neurons and the astrocytic tubes. Some of these interactions are known. For example, the astrocytes in the RMS not only physically separate the chains of new neurons from the surrounding parenchyma, but also control neuronal migration by taking up GABA secreted from the migrating neurons (**Bolteus and Bordey, 2004**), releasing an activating factor (**Mason et al., 2001**), trapping vascular endothelial cell-derived BDNF (**Snapyan et al., 2009**), and expressing nonsoluble factors (**Garcia-Marques et al., 2009**). However, little is known about how the tubular astrocytic structures are maintained or how their interactions with migrating neurons are regulated.

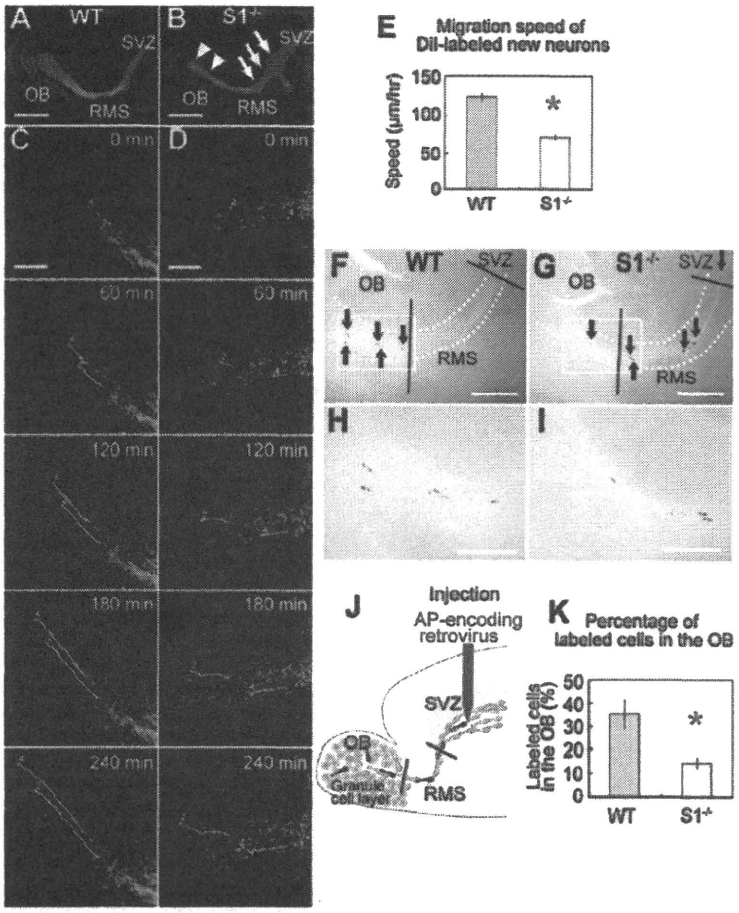

Figure 1. New Neuron Migration in the RMS of *S1*$^{-/-}$ Mice

(A and B) Hoechst-stained sagittal brain sections including the RMS of P7 WT (A) and *S1*$^{-/-}$ (B) mice. In the *S1*$^{-/-}$ brain, cells accumulated within the anterior part of the SVZ and proximal part of the RMS (arrows), whereas the distal part of the RMS and its extension inside the OB (arrowheads) were thinned.

(C–E) Time-lapse sequence of DiI-labeled cells migrating in the RMS of WT (C) and *S1*$^{-/-}$ (D) brain slices (OB is to left). Four cells in each slice are labeled (1, blue; 2, light green; 3, red; 4, cyan) in the 0 min panel, and their tracks over time are indicated by lines of the same color. The mean migration speed of DiI-labeled cells in the *S1*$^{-/-}$ RMS (yellow bar) was significantly slower than in the WT RMS (gray bar) (E, $p < 0.0001$).

(F–K) AP staining of WT (F) and *S1*$^{-/-}$ (G) brains 3 days after AP-encoding retroviral injection into the anterior SVZ (J). Arrows in (F) and (G) indicate AP-labeled migrating new neurons in the SVZ-RMS-OB pathway (between broken lines). Black lines indicate the boundaries of the SVZ, RMS, and OB. (H) and (I) are higher-magnification images of the boxes in (F) and (G), respectively. The percentage of AP-labeled cells inside the OB was significantly lower in the *S1*$^{-/-}$ than the WT brain (K, $p = 0.0011$). Error bars indicate ±SEM. Scale bars: 2 mm (A and B), 1 mm (F and G), 500 μm (H and I), 200 μm (C and D). See also Movie S1.

The Slit proteins, large diffusible proteins whose receptors are the Robo transmembrane proteins, guide extending axons and migrating neurons in the CNS through chemorepulsion (**Andrews et al., 2006, 2007; Brose et al., 1999; Marín et al., 2003; Nguyen Ba-Charvet et al., 1999; Plump et al., 2002; Wu et al., 1999**). Slit1 and Slit2 are expressed in periventricular tissue and repel new neurons (**Hu, 1999; Hu and Rutishauser, 1996; Wu et al., 1999**). Slit1 is also expressed by the neurons migrating in the SVZ-RMS-OB pathway, and it appears to have a cell-autonomous role in their migration (**Nguyen-Ba-Charvet et al., 2004**).

We show here an unexpected mechanism that the new neurons use to support their long-distance directional migration in the adult brain. Our results reveal that the RMS astrocytes express Robo receptors and respond to the repulsive activity of the neuron-secreted Slit by forming and maintaining glial tubes.

RESULTS

New Neuron Migration Is Disturbed in the RMS of *Slit1* Knockout Mice

We first examined the morphology of the mouse SVZ-RMS-OB pathway in Hoechst-stained sagittal sections (**Figures 1A and 1B**). In Slit1-deficient (*S1*$^{-/-}$) mice, the anterior part of the SVZ and proximal part of the RMS were thickened, whereas the distal (rostral) part of the RMS was thinned. We quantified the number of proliferating and apoptotic cells throughout the RMS pathway by labeling cells for BrdU incorporation and cleaved caspase-3, respectively. There were no significant differences in these values between the WT and *S1*$^{-/-}$ brains (BrdU: WT, 4440 ± 374 cells versus *S1*$^{-/-}$, 5296 ± 497 cells, $p = 0.231$; cleaved caspase-3: WT, 203 ± 44 cells versus *S1*$^{-/-}$, 242 ± 27 cells, $p = 0.434$), suggesting that the loss of Slit1 did not affect the proliferation or survival of the cells in this region. However, the new neurons apparently accumulated in the anterior SVZ and proximal RMS of the *S1*$^{-/-}$ mice.

To examine the migration defects of the new neurons in the *S1*$^{-/-}$ RMS, we compared their movement in *S1*$^{-/-}$ and WT brain slices in culture (**Figures 1C–1E**). To observe the migrating neurons, a DiI crystal was applied to the posterior part of the RMS in sagittal brain slices containing the SVZ-RMS-OB pathway. Time-lapse recordings of the DiI-labeled cells in the WT brain slices revealed that most neurons migrated rapidly along the RMS toward the OB, as previously reported (**Murase and Horwitz, 2002**). However, in slices prepared from *S1*$^{-/-}$ mice, the migration of the DiI-labeled cells was significantly slower (40% reduction in speed) (**Figures 1C–1E and Movie S1**).

To investigate the effects of the *Slit1* mutation on neuronal migration in vivo, we stereotaxically injected a recombinant retrovirus encoding alkaline phosphatase (AP) into the anterior part of the SVZ and counted the number of labeled cells in the SVZ, RMS, and OB 3 days later (**Figures 1F–1K**). There was no

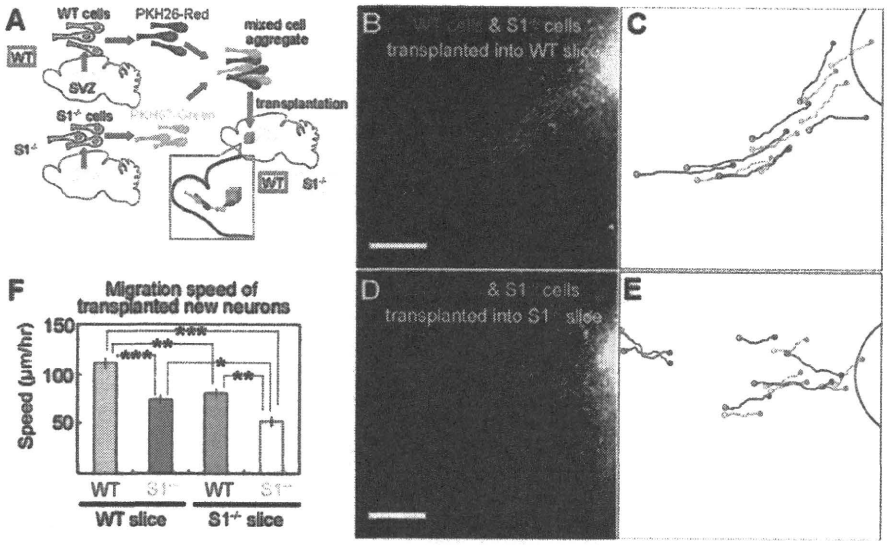

Figure 2. Migration of WT and *S1*$^{-/-}$ Cells Transplanted into WT and *S1*$^{-/-}$ Brain Slices

(A) Schematic drawing of the experimental protocol. New neurons dissociated from WT and *S1*$^{-/-}$ SVZs were labeled with different fluorescent dyes, red (PKH-26) for WT and green (PKH-67) for *S1*$^{-/-}$, mixed into cell aggregates, and transplanted into the anterior SVZ of WT and *S1*$^{-/-}$ sagittal brain slices. The migration of the labeled cells was recorded by two-color time-lapse imaging.

(B–E) PKH-labeled transplanted WT (red) and *S1*$^{-/-}$ (green) cells migrating in a WT (B) or *S1*$^{-/-}$ (D) brain slice. Scale bars indicate 200 μm. OB is to the left. The cell tracks during 4 hr of monitoring are shown by the colored lines in (C) (WT) and (E) (*S1*$^{-/-}$) (closed circles, cell positions at 0 min; open circles, positions at 240 min).

(F) Mean speed of migration of WT and *S1*$^{-/-}$ new neurons transplanted into WT (gray bar, WT cells; dark green bar, *S1*$^{-/-}$ cells) or *S1*$^{-/-}$ RMS (orange bar, WT cells; yellow bar, *S1*$^{-/-}$ cells). Compared with the speed of WT cells transplanted into WT slices, the speed of *S1*$^{-/-}$ cells transplanted into WT slices ($p < 0.0001$) and WT cells transplanted into *S1*$^{-/-}$ slices ($p = 0.0002$) was significantly reduced. The *S1*$^{-/-}$ cell migration speed was even slower in *S1*$^{-/-}$ slices (*S1*$^{-/-}$ cells in WT RMS versus *S1*$^{-/-}$ cells in *S1*$^{-/-}$ RMS: $p = 0.0041$, WT cells in *S1*$^{-/-}$ RMS versus *S1*$^{-/-}$ cells in *S1*$^{-/-}$ RMS: $p = 0.0007$). *$p < 0.05$, **$p < 0.01$, ***$p < 0.001$. Error bars indicate ±SEM. See also **Movie S2**.

significant difference in the total number of AP-labeled cells in the brains of the WT and *S1*$^{-/-}$ mice, indicating that Slit1 deficiency does not affect the infection or proliferation of the new neurons in the SVZ and RMS. However, the proportion of cells that reached the OB was significantly reduced in the *S1*$^{-/-}$ mice (**Figure 1**K). Together, these results clearly indicated that the migration of new neurons to the OB was disturbed in the *S1*$^{-/-}$ brain.

Efficient Migration through the RMS Requires Cell-Autonomous and Non-Cell-Autonomous Effects of Slit1 Expressed by the Migrating New Neurons

To examine whether it is necessary for a new neuron to express Slit1 for its own migration, we compared the migratory behavior of WT and *S1*$^{-/-}$ new neurons labeled with different fluorescent dyes (red for WT and green for *S1*$^{-/-}$) in the RMS of WT brain slices, by two-color time-lapse recording (**Figure 2**). *S1*$^{-/-}$ cells transplanted into the *S1*$^{-/-}$ RMS (**Figures 2**D and 2E, green) showed slower migration than WT cells transplanted into the WT RMS (**Figures 2**B and 2C, red), similar to the cells labeled with DiI in the WT and *S1*$^{-/-}$ brain slices (**Figures 1**C and 1D). *S1*$^{-/-}$ new neurons migrating in the WT RMS also showed significantly slower speeds compared with Slit1-expressing WT cells (**Figures 2**B, 2C, and 2F). Thus, for rapid migration, the new neurons appeared to require Slit1 in a cell-autonomous manner. We next examined whether Slit1-expressing WT cells could migrate normally in a Slit1-deficient RMS (**Figures 2**D and 2E) by transplanting mixed aggregates of WT and *S1*$^{-/-}$ cells into a *S1*$^{-/-}$ brain slice. The WT cells in the *S1*$^{-/-}$ RMS (**Figures 2**D and 2E, red) showed slower and more irregular migration than those in the WT RMS (**Figures 2**B and 2C, red), suggesting that the normal migration of new neurons also required Slit1 expression by the surrounding new neurons (**Movie S2**).

We also tested whether the two dyes used in this experiment affected the new-neuron migration differently. WT cells were labeled with either the red or green fluorescent dye and transplanted into WT brain slices, but there were no significant differences in the migratory behaviors of the two groups of cells (data not shown).

Taken together, these results indicated that Slit1 derived from both the new neurons themselves and the surrounding new neurons in the RMS is necessary to regulate the migration of new neurons to the OB.

Robo Proteins Are Expressed in Migrating New Neurons and in the Surrounding Astrocytes in the RMS

We next sought to identify the cells expressing Slit's receptors, the Robo proteins, in the RMS. To compare the pattern of Robo expression with that of Slit1, brain sections of heterozygous *Slit1*-GFP knockin (**Nguyen-Ba-Charvet et al., 2004; Plump et al., 2002**) (**Figure 3**A) and WT (**Figures 3**B–3G) mice were stained using Robo1-, Robo2-, and Robo3-specific antibodies

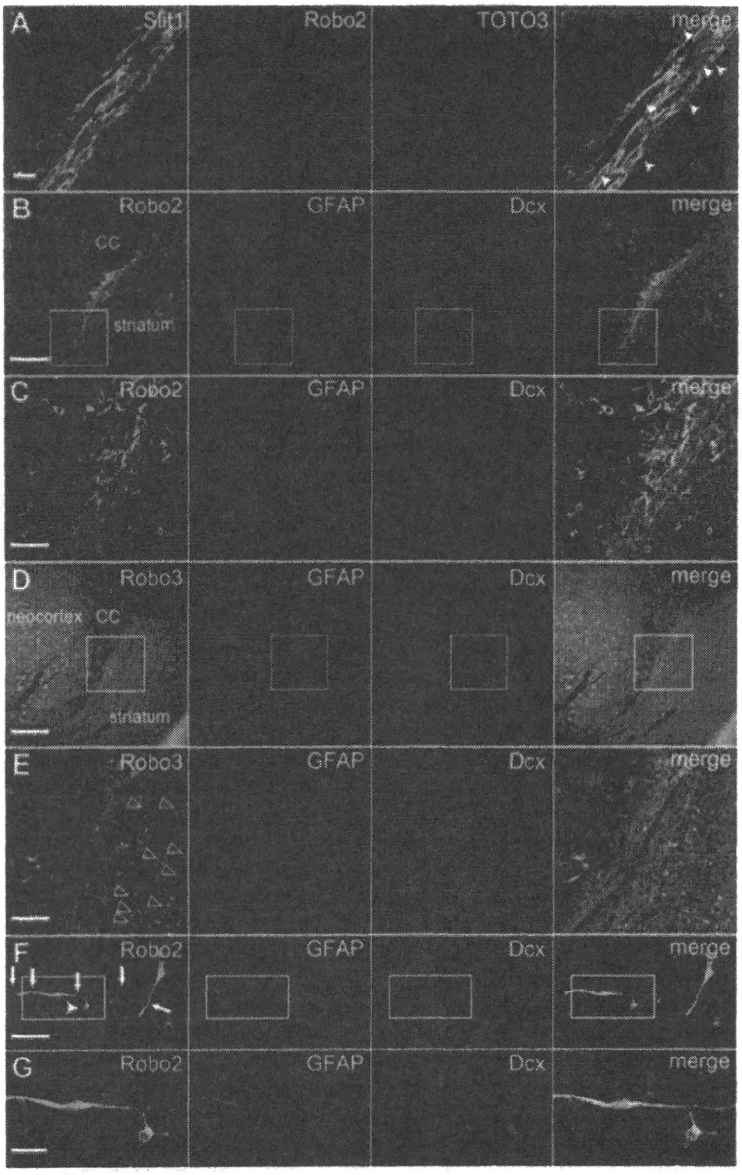

Figure 3. Localization of Robo2 Protein in the RMS

(A) Slit1/GFP and Robo2 immunohistochemistry in the RMS. Slit1/GFP (green) was localized to chain-forming new neurons in the RMS. Robo2 (red) protein was also detectable along the RMS, including in new neurons. Note that the Robo2+ processes with astrocytic morphology surrounding the chains of new neurons were negative for Slit1 (arrowheads). The nuclei were stained with TOTO3 (blue).

(B and C) Robo2 immunohistochemistry in the RMS. Robo2 protein (green) was detectable all along the RMS (B). High-magnification images. Boxed area in (B) shows that Robo2 (green) was strongly detected in the GFAP+ (red) astrocytic soma and processes and weakly in the Dcx+ (blue) new neurons (C).

(D and E) Robo3 immunohistochemistry in the RMS (E) is a high-magnification image of the boxed area in (D). Robo3 protein (green) was strongly detected in neurons in the neocortex and striatum (open arrowheads in E) and more weakly in the RMS. Within the RMS, the immunoreactivity of astrocytic processes (red) was easily detected, whereas that of new neurons (blue) was faint.

(F and G) Immunocytochemistry of cultured SVZ/RMS cells dissociated from adult WT mice. Robo2 (green) was localized to the GFAP+ (red) processes (arrows) and the soma of astrocytes, and to Dcx+ (blue) new neurons (arrowhead) (F). High-magnification images of the boxed area in (F) are shown in (G).

Scale bars: 200 μm (B and D), 50 μm (C, E, and F), 20 μm (A and G).

(**Tamada et al., 2008**). As previously reported (**Nguyen-Ba-Charvet et al., 2004**), the chain-forming new neurons in the SVZ and RMS expressed Slit1/GFP (green). They also expressed Robo2 (red), as expected (**Long et al., 2007**; **Nguyen-Ba-Charvet et al., 2004**). In addition, stronger Robo2 immunoreactivity was observed in Slit/GFP-negative cells in the RMS. Double immunostaining of Robo2 with cell-specific markers for new neurons (Dcx) and astrocytes (GFAP) showed that Robo2 was expressed strongly in the processes and soma of the astrocytes forming the glial tubes and weakly in the new neurons (**Figures 3**B and 3C). Furthermore, the astrocytic expression of Robo2 was observed almost exclusively in the SVZ-RMS-OB pathway and the corpus callosum overlying the SVZ and was undetectable in the hippocampus and neocortex (data not shown). Because it was difficult to distinguish the processes of new neurons from those of astrocytes in the RMS, where they were tightly associated, we confirmed the above expression pattern using dissociated SVZ cells plated on coverslips. We clearly observed Robo2 protein in the soma and processes of both astrocytes and new neurons (**Figures 3**F and 3G).

Consistent with a previous report on the localization of *Robo1* mRNA (**Nguyen-Ba-Charvet et al., 2004**), we did not detect Robo1 protein in the SVZ or RMS (data not shown). Robo3 was detected in the new neurons and astrocytes in the RMS, but its expression was stronger in the mature neurons of the neocortex and striatum (**Figures 3**D and 3E). In summary, the ligand Slit1 was expressed in the migrating new neurons, whereas its receptors Robo2 and Robo3 were expressed in both the new neurons and astrocytes. These expression patterns suggest that Slit-Robo signaling is involved in the interaction between new neurons and their surrounding astrocytes in the RMS and is not simply a directional cue for migrating neurons.

Cellular Organization of the RMS Is Disrupted in *S1*$^{-/-}$ Mice

To investigate whether Slit-Robo signaling affects the cellular organization of the RMS, sagittal and coronal sections of *S1*$^{-/-}$ and WT mouse brains were immunostained with antibodies to

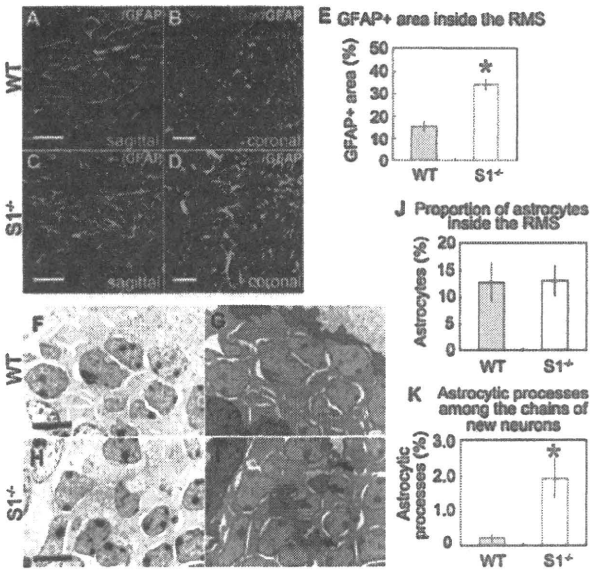

Figure 4. Cellular Organization of the RMS in *S1*$^{-/-}$ Mice

(A–E) Confocal images of the RMS of WT (A and B) and *S1*$^{-/-}$ (C and D) mice stained with Dcx (red) and GFAP (green). Sagittal sections of the WT RMS showed GFAP+ (green) astrocytic processes parallel to Dcx+ (red) new-neuron chains (A). The *S1*$^{-/-}$ RMS showed more, thick GFAP+ processes with irregular orientations, occasionally running across the chains (C). Coronal slices of WT RMS (B) showed cross-sections of thin GFAP+ astrocytic processes between clusters of Dcx+ neurons. The *S1*$^{-/-}$ RMS (D) showed many longitudinal sections of thick GFAP+ processes among the new neurons. Quantification of the GFAP+ area in the RMS showed that Slit1 deletion caused a significant increase in the amount of astrocytic processes within the RMS (E, $p = 0.0012$).

(F–K) Ultrastructural organization of the WT (F and G) and *S1*$^{-/-}$ (H and I) RMS, according to the criteria described in **Experimental Procedures**. New neurons (dark cytoplasm) and astrocytes (light cytoplasm) are indicated by red and blue, respectively (G and I). The percentage of astrocyte cell bodies in the RMS was not significantly different between the two groups (J, $p = 0.9558$); however, the astrocytic processes within chains were significantly more frequent in the *S1*$^{-/-}$ RMS (I, arrows) compared to controls (G). The area occupied by astrocytic processes inside the chains of new neurons was significantly increased in the *S1*$^{-/-}$ RMS (K, $p = 0.0409$).

Error bars indicate ±SEM. Scale bars: 50 μm (A and C), 20 μm (B and D), 5 μm (F–I). See also **Figure S1**.

GFAP and Dcx. Although new neurons accumulated in the *S1*$^{-/-}$ SVZ and RMS (**Figure 1B**), they still formed elongated chain-like aggregates, some of which were closely associated with adjacent blood vessels, much as in WT brains (**Snapyan et al., 2009**) (**Figures S1A** and S1B). However, the distribution and directionality of the astrocytic processes were altered in the *S1*$^{-/-}$ RMS (**Figures 4A–4D**). In the WT RMS, most of the astrocytic processes were oriented parallel to the chains of migrating new neurons. In contrast, irregular astrocytic processes were frequently observed running across the chains of new neurons in the *S1*$^{-/-}$ RMS. The proportion of the area inside the RMS occupied by GFAP+ processes in the *S1*$^{-/-}$ brains was more than twice that in the WT brains (**Figure 4E**).

To corroborate and extend this observation at higher resolution, we used electron microscopy. As described previously (**Doetsch et al., 1997**; **Jankovski and Sotelo, 1996**), the processes of astrocytes could be identified at the ultrastructural level by their light cytoplasm, which contained glycogen granules. They were readily distinguishable from the processes of new neurons in the RMS, which had a dark cytoplasm and contained many ribosomes (**Figures 4F–4I**). There was no significant difference in the percentage of astrocytic cell bodies among the identified cells in the RMS between the WT and *S1*$^{-/-}$ brains (**Figure 4J**). However, in the *S1*$^{-/-}$ RMS, astrocytic processes were observed within aggregates of new neurons. Such intermingling was rarely seen in the WT RMS (**Figure 4K**). The disorganization of glial tubes in the *S1*$^{-/-}$ RMS suggests that the Slit1 secreted by new neurons may facilitate their migration by actively preventing astrocytic processes from invading the migratory conduits within chains.

Slit Repels SVZ/RMS Astrocytes

The astrocytic expression of Robos (**Figure 3**) combined with the disorganization of the astrocytic tubes in Slit-deficient mice (**Figure 4**) strongly suggested that Slit can directly control the organization of astrocytes. To test this possibility, we performed an in vitro repulsion assay using a Slit-expressing HEK cell line (**Wu et al., 1999**) and primary cultured astrocytes dissociated from the SVZ and RMS. First, we examined the effect of Slit on the proliferation and survival of the astrocytes by culturing the astrocytes for 48 hr with conditioned medium from either Slit-expressing HEK cells or control, non-Slit-expressing HEK cells. The astrocytes were then double stained for GFAP and a mitotic cell marker, Ki67, or an apoptotic cell marker, cleaved caspase-3. There was no significant difference in the number of GFAP+ cells, i.e., astrocytes, or in the percentage of astrocytes expressing Ki67 or cleaved caspase-3 between the two culture conditions (data not shown), suggesting that Slit does not affect the proliferation or survival of SVZ/RMS astrocytes.

We next tested the effects of Slit on the migration of these astrocytes. For this purpose, the astrocytes were cocultured on plastic plates with small pieces of collagen gel containing Slit-expressing HEK cells or control HEK cells (**Figures 5A–5C**). After 4 days of culture, the distribution of astrocytes on the edges of the gel pieces was compared between the Slit and control groups. To quantify the GFAP+ cells, we measured the 500 μm wide strip just inside the edge of the gel piece and compared the GFAP+ area with the total area of the strip. Significantly fewer astrocytes lay on the Slit-containing gels than on the non-Slit-containing gels (**Figures 5B–5D**), suggesting that the astrocytes were repelled by Slit.

To investigate whether this repulsive effect of Slit was mediated by the Robo receptors expressed on the astrocytes, we used a dominant-negative form of Robo1 (Robo DN), which lacks the intracellular domains required for signal transduction (**Hammond et al., 2005**; **Shiau et al., 2008**) (**Figures 5E–5K**). The Robo DN-transfected SVZ/RMS astrocytes showed no significant change in proliferation, apoptosis, or Slit-independent migration activity compared with control astrocytes transfected with a vector encoding GFP (**Figures S2A–S2I**). However, compared with the controls (**Figures 5F**, 5G, and 5J), the Robo DN-transfected astrocytes were considerably less affected by Slit (**Figures 5H**, 5I, and 5K). Moreover, *Robo2* or *Robo3* knockdown

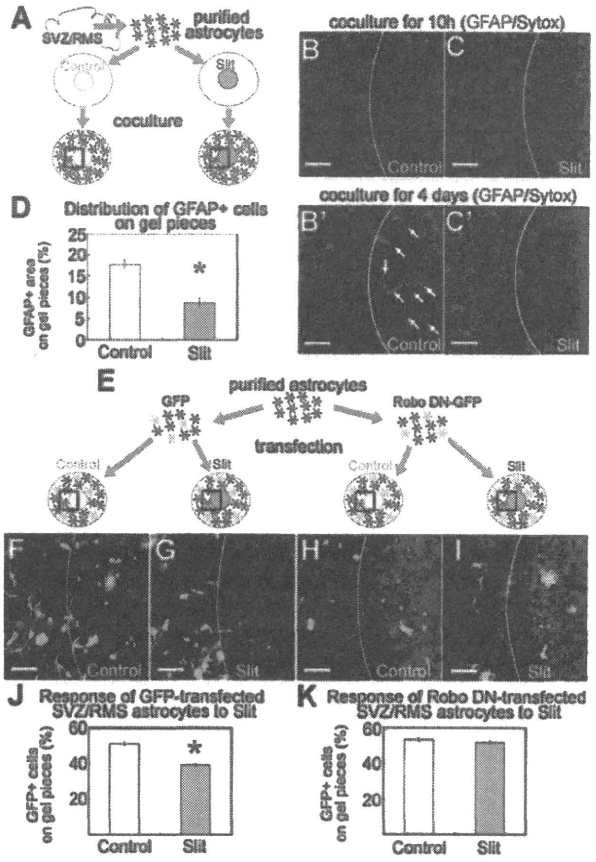

Figure 5. Repulsive Activity of Slit for Cultured Astrocytes

(A-D) SVZ/RMS astrocytes were cocultured with Slit-secreting (pink) and control (pale green) HEK cells mixed with collagen gel (A). Boxes in (A) indicate the magnified area shown in (B) and (C). After 10 hr, most astrocytes were attached to the dish and had short processes; few were on gel pieces containing control (B) or Slit-expressing (C) HEK cells. After 4 days, several astrocytes had migrated onto the pieces containing control HEK cells (B–B′, arrows), but significantly fewer onto those containing Slit-secreting (C–C′) HEK cells. The proportion of the 500 μm wide strip just inside the edge of the gel piece that was GFAP+ was quantified (D, $p = 0.0094$).

(E–K) Effects of Slit on astrocytes transfected with dominant-negative Robo (Robo DN). Cultured astrocytes dissociated from the SVZ and RMS were transfected with GFP-tagged Robo DN (H and I) or GFP (F and G), then cocultured with Slit-secreting or control HEK cells in collagen gel for 60 hr (E). Images show GFP+ cells near the edge of the control (F and H) and Slit-containing (G and I) HEK-cell-mixed gel. Graph shows the percentage of GFP+ GFAP+ astrocytes on the gel within 500 μm of its edge divided by the number in the 1000 μm wide space from 500 μm inside to 500 μm outside the gel border (J and K). The percentage of GFP-transfected astrocytes was significantly lower on Slit-containing gel pieces than on controls (J, $p = 0.0026$). This difference was not seen using astrocytes transfected with Robo DN-GFP (K).

Error bars indicate ±SEM. Scale bars: 200 μm. See also Figure S2.

by an shRNA-encoding lentivirus also suppressed the repulsive activity of Slit (Figures S2J–S2R), suggesting that Robo2 and Robo3 mediated the repulsion of the astrocytes by Slit, at least in part.

We further examined the possibility that neuronal Robos influences the arrangement of the astrocytes (Figures S2S–S2Z). To knock down the *Robo2* and *Robo3* specifically in new neurons, new neurons dissociated from a P0-2 mouse SVZ were infected with lentiviruses encoding either *Robo2* shRNA, *Robo3* shRNA, or a control sequence. The new neurons infected with each virus were then drop-cultured, mixed with astrocytes, and plated as aggregates on a laminin-coated dish. Twenty-four hours later, the new neurons had migrated out of the aggregates to a similar extent, regardless of the *Robo* knockdown or *Slit1* knockout (data not shown). Subsequently, the astrocytes began to extend their processes along the WT migrating new neurons (Figures S2S and S2T). Notably, the migration of *Slit1*$^{-/-}$ new neurons associated with astrocytes was significantly disturbed (Figures S2U and S2V). Consistent with our in vivo observation (Figures 4A–4D), the normal arrangement of the astrocytic processes was markedly disrupted when they were cocultured with Slit1-deficient new neurons (Figures S2U and S2V), further confirming our conclusion that neuronal Slit1 is required for the astrocytic arrangement. On the other hand, we did not observe any such disturbance in astrocytes cocultured with new neurons infected with lentiviruses encoding *Robo2* or *Robo3* shRNA (Figures S2W–S2Z). Taken together, these results suggest that the neuron-derived repulsive factor Slit1 and its receptors that are expressed on astrocytes, rather than on neurons, directly control the organization of the glial tube.

Newly Generated Neurons Control the Morphology of SVZ/RMS Astrocytes to Promote Their Own Migration

Finally, using new-neuron-astrocyte cocultures and time-lapse imaging, we studied the role of Slit-Robo signaling in the astrocytic control of neuronal migration and in the neuron-induced morphological changes in SVZ/RMS astrocytes. Aggregates of SVZ new neurons from WT or *S1*$^{-/-}$ mice were placed on plastic dishes with or without SVZ/RMS astrocytic feeder layers. On the dishes without astrocytes, there was no significant difference in the distance or speed of migration between *S1*$^{-/-}$ and WT new neurons (Figures 6A, 6B, 6E, S3A, S3D, and S3G). However, when *S1*$^{-/-}$ new neurons were plated on a monolayer of astrocytes, they migrated significantly more slowly than WT new neurons (Figures 6C, 6D, 6F, S3B, S3C, S3E, S3F, and S3H). This result suggested that Slit1's promotion of neuronal migration depends on astrocytes.

To test whether the Slit1-expressing neurons directly induced morphological changes in astrocytes, we observed the astrocytes making contact with new neurons, by z-stack time-lapse imaging of genetically labeled new neurons (*Dcx-DsRed*; Wang et al., 2007) and astrocytes (*Gfap-EGFP*) cocultured in a 3D gel. Under these conditions, the cells were suspended and freely moving in 3D space, which better mimics the in vivo physical environment than does monolayer culture. Interestingly, furrows formed on the astrocytes' membrane where they contacted the migrating new neurons (arrows in Figures 7A–7C and Movie S3). To examine whether astrocytes making contact with new neurons displayed a similar morphology in vivo, we observed the 3D structure of the glial tubes surrounding the chains of new neurons by the confocal imaging of serial optical sections taken from the whole-mount SVZ. Using *Gfap-EGFP* mice, we

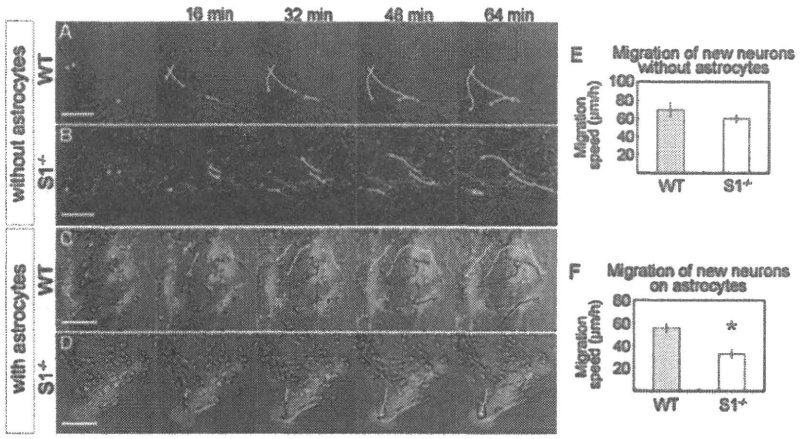

Figure 6. Slit1-Robo-Dependent Migration of New Neurons on Astrocytes

Migration speed of new neurons on an astrocytic feeder layer. Time-lapse sequence of WT (A) and $S1^{-/-}$ (B) new neurons migrating on the surface of plastic dishes without astrocytes. Representative tracks of the migrating new neurons indicated by dots and lines showed no significant difference in the migration speed between the two groups (E, $p = 0.2850$). Time-lapse sequence of WT (C) and $S1^{-/-}$ (D) new neurons migrating on astrocytes dissociated from the SVZ/RMS of *Gfap-EGFP* mice. The tracks of representative cells indicated by dots in the first panels are shown by lines in the following panels (16 min, 32 min, 48 min, 64 min). The migration speed of $S1^{-/-}$ new neurons on astrocytes was significantly reduced compared with that of WT new neurons (F, $p = 0.0012$).

Error bars indicate ±SEM. Scale bars: 50 μm. See also **Figure S3**.

could visualize the morphology of the astrocytic membrane in contact with new neurons. The membrane of astrocytes formed clear invaginations with a size and shape that could accommodate the rounded outline of the chains of new neurons (**Figure S4A**), consistent with the observations in cultured cells (**Movie S3**). We further examined the fine morphology of the contact sites of the astrocyte membrane with new neurons by EM analyses. Close examination of coronal RMS sections revealed clear invaginations in the cell bodies of astrocytes along the contours of chain-forming new neurons (**Figures S4B–S4E**).

To determine whether these dynamic morphological changes were mediated by the Robo receptors on the astrocytes, aggregates of SVZ new neurons were placed on a monolayer of astrocytes transfected with either GFP-tagged Robo DN or GFP

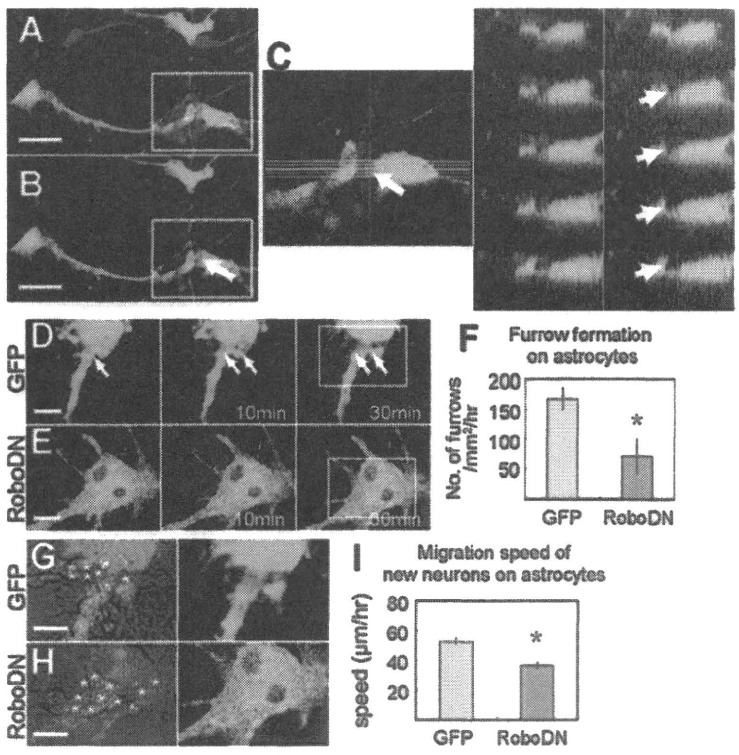

Figure 7. Dynamic Morphological Changes of Astrocytes Associated with Neuronal Migration

(A–C) New neurons (*Dcx-DsRed*) and SVZ/RMS astrocytes (*Gfap-EGFP*) were cocultured in 3D matrices (A). New neurons (red) migrated along the processes of astrocytes (green), on which furrows occasionally formed (B, arrows). A higher-magnification image of the boxed area in (A) is shown in (C). At right, a series of X-Z sections of the furrow on an astrocyte at the positions indicated by the green lines shown in the panel at left.

(D and E) Time-lapse recording of furrow formation. Middle and right panels show images captured 10 and 30 min after the left one. When new neurons migrated on a monolayer culture of SVZ/RMS astrocytes transfected with a control vector encoding GFP (D), the astrocytes changed their shape, occasionally forming furrows on the membrane in contact with the new neurons (arrows). Such morphological changes were suppressed in astrocytes transfected with dominant-negative Robo1 (Robo DN) (E).

(F) Quantification of the furrows. Graph shows the number of furrows formed on 1 mm^2 of the astrocyte membrane surface per hour, which was significantly reduced for astrocytes transfected with Robo DN compared with control-vector-transfected astrocytes ($p = 0.0254$).

(G and H) Higher-magnification images of the boxed regions in (D) and (E), respectively. The migration of new neurons (asterisks) over astrocytes was frequently associated with the formation of furrows on the membrane of astrocytes transfected with the control vector (G) but not with Robo DN (H).

(I) The migration speed of new neurons on Robo-DN-transfected astrocytes was significantly decreased compared with that on GFP-transfected astrocytes ($p < 0.0001$).

Error bars indicate ±SEM. Scale bars: 20 μm. See also **Figure S4** and **Movies S3, S4, and S5**.

alone, and the morphology of these astrocytes was recorded. Similar furrows were formed on the membrane of both types of astrocytes where they contacted the migrating new neurons, but at a significantly lower frequency in the Robo DN-expressing astrocyte culture than in the control one (**Figures 7D–7F** and **Movie S4**). There was no significant difference in the spontaneous movement of the Robo DN-expressing and control astrocytes, suggesting that Robo DN does not affect general morphological changes in astrocytes that are not mediated by Slit-Robo signaling. New neurons from $S1^{-/-}$ mice induced similar furrows, but again at a significantly lower frequency than WT neurons (**Figures S4F–S4H**). These data suggested that the Slit secreted by migrating new neurons induces cell-shape changes in astrocytes through Robo signaling.

We then compared the speed of the new neurons migrating on Robo DN-expressing and control astrocytes. The mean migration speed of the new neurons on Robo DN-expressing astrocytes was significantly lower than on control astrocytes (**Figures 7G–7I**). Taken together, these results suggest that the Slit1 secreted by new neurons alters the morphology of astrocytes through the astrocytes' Robo receptors, thereby promoting the fast migration of new neurons in contact with the astrocytes.

DISCUSSION

Cell migration is controlled by extracellular cues within and near the cell's path. Here, we present evidence that the young neurons in the RMS of the adult brain help maintain an environment that is permissive for their own migration by actively modifying the astrocytic morphology.

In the embryonic neocortex, immature neurons are generated from precursors in the cortical ventricular zone and SVZ and migrate along radial glial fibers to populate the cortical plate (**Hatten, 2002**; **Marín and Rubenstein, 2003**; **Miyata et al., 2001**; **Rakic, 1971**; **Rakic, 1972**). The formation and maintenance of radial glia is partly controlled by signals from the migrating neurons (**Anton et al., 1997**; **Schmid et al., 2003**; **Zheng et al., 1996**), suggesting that the migrating neurons in the developing brain help regulate the morphology and function of cells along their migration route. However, the molecular mechanisms and dynamic anatomical changes used by the new neurons to regulate their migratory microenvironment have not been elucidated.

The postnatal brain offers unique opportunities for studying how young neurons regulate their migratory environment. Since the migratory routes are very long compared to those in the embryo, the migrating cells often have to navigate very complex territories, and migration is not a transitory phenomenon, but one that occurs throughout life. The long-distance migration of new neurons occurs in the SVZ-RMS-OB pathway in adult rodents and other mammals. Radial glia disappear within the first few postnatal days, and complex circuits of neuronal fibers and vasculature subsequently develop, accompanied by rapid increases in the numbers of other glial cells, including astrocytes. Therefore, new neurons in the adult brain migrate through densely packed tissue without the assistance of radial glia. Instead, SVZ-RMS new neurons migrate along one another, forming chains within glial tubes formed by astrocytes (**Doetsch and Alvarez-Buylla, 1996**; **Jankovski and Sotelo, 1996**; **Lois et al., 1996**; **Wichterle et al., 1997**). The glial tubes largely separate the chains of new neurons from the surrounding brain parenchyma, which helps to maintain the migration route. Genetic defects in glial tube formation have been reported, and these defects coincide with the abnormal migration of new neurons (**Anton et al., 2004**; **Belvindrah et al., 2007**; **Chazal et al., 2000**; **Ghashghaei et al., 2006**). However, the precise molecular interactions between SVZ-RMS migrating new neurons and their surrounding astrocytes have not been determined. Here, we showed that signaling between new neurons, which secrete Slit1 (**Nguyen-Ba-Charvet et al., 2004**), and astrocytes, which express Robo receptors, is critical for both the migration of new neurons and the formation and maintenance of the astrocytic tunnels.

The new neurons in $S1^{-/-}$ mice were reported to have defects in chain formation and directional migration in the SVZ and RMS (**Nguyen-Ba-Charvet et al., 2004**). Using time-lapse recording of migrating new neurons in the RMS of organotypic cultures and retroviral labeling of new neurons in vivo, we directly demonstrated that $S1^{-/-}$ new neurons migrate significantly more slowly than WT new neurons (**Figure 1**). We also showed that WT new neurons failed to migrate efficiently when placed in the RMS of a $S1^{-/-}$ brain (**Figure 2**). In the $S1^{-/-}$ brain, new neurons formed chains surrounded by glial tubes, but the morphology and arrangement of the astrocytic processes were significantly affected (**Figure 4**). These phenotypes suggested that Slit1 is involved in the formation and maintenance of glial structures that are permissive for normal long-range neuronal migration.

It is generally accepted that Slit proteins assist in the directional migration of new neurons born in the adult SVZ: Slit1 and Slit2 secreted from the choroid plexus and the septum direct neurons rostrally, toward the OB (**Hu, 1999**; **Hu and Rutishauser, 1996**; **Sawamoto et al., 2006**; **Wu et al., 1999**). Therefore, we expected that receptors for Slit would be expressed by the migrating new neurons. However, although the young neurons expressed low levels of the Robos, Robo2 and Robo3 were strongly expressed by the astrocytes forming the glial tubes (**Figure 3**), suggesting that the Slits might also play a role in organizing astrocytes along the migration route. Consistent with this possibility, inhibiting the Robo signal in astrocytes, but not in neurons, decreased Slit's effect on the morphology and arrangement of astrocytes (**Figures 7** and **S2S–S2Z**). The knockout of *Slit1* or knockdown of *Robo* in new neurons cultured without astrocytes did not affect their migration (**Figures 6**, **S2W–S2Z**, **S3A**, S3D, and S3G). However, we cannot rule out the possibility that the absence of Slit1 directly affects the migration of new neurons, as previously reported (**Nguyen-Ba-Charvet et al., 2004**), because there are several methodological differences between our study and theirs. Instead, our results demonstrate a mechanism by which neuronal Slit1 affects astrocytes rather than new neurons in the formation and maintenance of glial structures that permit normal, long-range neuronal migration.

Using cultured astrocytes dissociated from the SVZ and RMS, we found that the Slits are a potential chemorepellent for SVZ/RMS astrocytes. Slits altered the distribution of astrocytes in the culture dish by a process that depended on the presence of Robo receptors (**Figure 5**). The endogenous Slit1 from new neurons did not completely "repel" the cell body of astrocytes,

possibly because the concentration of Slit1 produced by the new neurons was not high enough. Instead, the Slit1 expression by new neurons directly affected the distribution and extension of astrocytic processes in the RMS (**Figure 4**). Moreover, we demonstrated that the SVZ/RMS astrocytes underwent dynamic morphological changes that were dependent on Robo function and the association with migrating new neurons expressing Slit1 (**Figures 6, 7**, and **S4F–S4H** and **Movie S4**). The transient elimination of migrating neurons by the infusion of an antiproliferative drug, Ara-C, resulted in disrupted astrocytic morphology, followed by reorganization of the glial tubes during neuronal regeneration (**Figures S4I–S4N**). Furthermore we observed dynamic morphological changes of astrocytes in whole-mount SVZ cultures (**Movie S5**). Therefore, the glial tubes are not static but can be dynamically remodeled by new neurons migrating in vivo. The observation that WT young neurons failed to migrate normally when grafted into the RMS of $S1^{-/-}$ mice (**Figure 2**) also suggests that an increased Slit1 concentration, resulting from its secretion by collections of new neurons in chains, may be required to exclude astrocytic processes from the neurons' migratory canal. Thus, the facilitation of migration by Slit1 within the SVZ and RMS may require the collective secretion of Slit1 by migrating neurons. Our demonstration that migrating new neurons control the morphology of astrocytes could help explain how groups of new neurons that have coalesced into chains migrate through a corridor that is largely devoid of astrocytic processes.

In conclusion, we report an aspect of neuronal chain migration, in which new neurons actively control the cellular environment of their own migratory route. Such a mechanism is likely to be more significant physiologically in the migration of adult-born neurons than in the radial glia-guided neuronal migration of the embryonic brain.

EXPERIMENTAL PROCEDURES

Animals

Wild-type (WT) ICR mice were purchased from SLC (Shizuoka, Japan). The *Slit1* mutant mice and *Dcx-DsRed* transgenic mice were described previously (**Plump et al., 2002**; **Wang et al., 2007**). *Gfap-EGFP* mice were obtained from the Mutant Mouse Regional Resource Center. In accordance with the national regulations and guidelines, all experimental procedures were reviewed by the Institutional Laboratory Animal Care and Use Committee and approved by the President of Nagoya City University.

Time-Lapse Analyses of New Neurons Migrating in Brain Slices

Organotypic brain slices were prepared from P7–P8 mice as reported previously (**Hirota et al., 2007**; **Murase and Horwitz, 2002**; **Suzuki and Goldman, 2003**) with modifications. Dissected brains were cut into sagittal slices (325 μm thick), then cultured on a filter membrane (Millipore, Billerica, MA, USA) submerged in Neurobasal medium (Invitrogen, Carlsbad, CA) supplemented with 10% FBS, 2 mM L-glutamine, 2% B-27 (Invitrogen), and 50 U/ml penicillin-streptomycin. Before starting the time-lapse recording, a DiI crystal was applied to the posterior part of the RMS, and the slice was cultured for 8–13 hr in 5% CO_2 at 37°C. For the transplantation experiments, the dissected SVZ and RMS of P5-6 WT and $S1^{-/-}$ mice were dissociated using trypsin-EDTA (Invitrogen). The dissociated WT and $S1^{-/-}$ cells were labeled using the PKH-26 and PKH-67 Fluorescent Cell Linker Kit (Sigma, St. Louis, MO), respectively, reaggregated by centrifugation, cut into pieces (200 μm in diameter), and implanted into the posterior part of the RMS. The slices were cultured for 20–28 hr before recording.

Time-lapse video recordings were obtained using an inverted Zeiss confocal microscope LSM5 PASCAL (Carl Zeiss, Oberkochen, Germany) equipped with a stage top microscope incubator INU-ZI-F1 (5% CO_2 at 37°C, Tokai Hit, Shizuoka, Japan) using a 10× dry objective lens. Every 10 min, eight to ten optical Z sections (Z-steps: 8–12 μm) were obtained automatically over a period of 5 hr, and all of the focal planes were merged. The migration speed of the cells was quantified using NIH ImageJ version 1.38 software.

Histological Analysis

Animals were deeply anesthetized and perfused intracardially with 0.9% saline, followed by 4% paraformaldehyde (PFA) in 0.1 M phosphate buffer. The brain was extracted, postfixed in the same fixative overnight, and cut into 50 μm coronal or sagittal sections on a vibratome (VT1200S, Leica, Heidelberg, Germany).

For immunostaining, the sections were incubated for 1 hr in blocking solution (10% donkey serum and 0.2% Triton X-100 in PBS) overnight at 4°C with the primary antibodies, which were diluted in the same solution, and for 2 hr at room temperature with Alexa Fluor-conjugated secondary antibodies (Invitrogen). Signal amplification was performed with biotinylated secondary antibodies (Jackson Laboratory, West Grove, PA) and the Vectastain Elite ABC kit (Vector Laboratories, Burlingame, CA), and the signals were visualized using the TSA Fluorescence System (PerkinElmer, Waltham, MA) or diaminobenzidine tetrahydrochloride (DAB). For nuclear staining, Hoechst, SYTOX-orange, SYTOX-green, or TOTO3 iodide (Invitrogen) was used.

BrdU Labeling and Tissue Processing

BrdU (50 mg/kg body weight, dissolved in PBS) was intraperitoneally injected into 10- to 12-week-old mice. One hour later, the brain was fixed and processed into 50 μm coronal sections. Following incubation in 2 N HCl at 60°C for 30 min, the sections were incubated in PBS containing 1% H_2O_2, then immunostained with a rat anti-BrdU antibody (1:200, Abcam).

Quantification

The sections were examined using a confocal laser microscope (LSM5 Pascal, Zeiss) or fluorescence microscope (BX-51, Olympus, Tokyo, Japan). The number of immunoreactive cells was counted in every sixth coronal section (BrdU) or in serial sagittal sections (cleaved caspase-3), at a magnification of 400×.

To analyze the cytoarchitecture of the RMS, two coronal sections (550 μm apart) that had been immunostained with anti-Dcx and anti-GFAP antibodies were selected, and images of the horizontal limb of the bilateral RMS from both sections were captured by confocal laser microscopy (20× dry objective lens, Zeiss). The captured images were measured to determine the proportion of the GFAP+ area inside the RMS, using ImageJ software.

Electron Microscopic Analysis

Animals were deeply anesthetized and perfused intracardially with 30 ml of 0.9% saline followed by 100 ml of 2% PFA-2% glutaraldehyde in 0.1 M phosphate buffer. The brain was extracted, post-fixed with the same fixative overnight, and the RMS was cut into 500 μm coronal sections on a vibratome (VT1200S, Leica). The sections were postfixed with 2% OsO_4 in 0.1 M phosphate buffer for 2 hr, block-stained in 1% uranyl acetate, dehydrated with a graded series of alcohol, and embedded in Epon 812 (TAAB, Reading, UK). Silver sections were then cut with an ultramicrotome (Leica UC6; Leica Microsystems, Vienna, Austria), stained with uranyl acetate and lead citrate, and observed with an electron microscope (H-7100; Hitachi, Tokyo, Japan).

Electron micrographs of the chains of new neurons in the RMS of WT ($n = 3$) and $S1^{-/-}$ ($n = 3$) mice were taken at random with a primary magnification of ×4000. The images were printed on projection papers at 2.9 times the primary magnification. All analyses were performed within the core of the RMS. The contours and nuclei of all the cells included in an image were traced and classified as previously described (**Doetsch and Alvarez-Buylla, 1996**; **Doetsch et al., 1997**; **Jankovski and Sotelo, 1996**) into new neurons, astrocytes, and others. New neurons were identified by their very electron-dense nuclei and cytoplasm, whereas astrocytes were identified by their electron-lucent nuclei and cytoplasm and the presence of glycogen granules. To quantify the astrocytic processes inserted among the chains of new neurons, a double lattice

test system with a 1.5 cm spacing was used (**Uchiyama and Watanabe, 1984**). All of the points inside the chains of new neurons were classified as being on new neurons, astrocytes, other cells, or undetermined structures, then the percentage of points falling on astrocytes was calculated.

Retrovirus Microinjection and Tissue Processing

Each animal was given stereotaxic injections of 0.8 μl (0.1 μl at each of eight locations) of replication-incompetent retroviruses encoding the marker gene human placental alkaline phosphatase (DAP) harvested from the psi2 DAP cell line (American Type Cell Culture 1949-CRL) (**Fields-Berry et al., 1992**) into the anterior SVZ of each hemisphere. Three days later, the brains were fixed as described above, cut into 50 μm sagittal serial sections, and processed for alkaline phosphatase (AP) histochemistry as previously described (**Fields-Berry et al., 1992**). The number of retrovirus-infected AP-stained (AP+) cells in the SVZ, RMS, and OB, respectively, was counted under 200× magnification.

Culture of SVZ/RMS Astrocytes

The SVZ and RMS were dissected from postnatal day 10 (P10)–P12 WT or *Gfap-EGFP* mice in L-15 medium (Invitrogen) and dissociated with trypsin-EDTA (Invitrogen). The dissociated cells were washed with L-15 medium, plated, and cultured with DMEM containing 10% FBS, 50 U/ml penicillin-streptomycin, and 2 mM L-glutamine. To purify astrocytes from the mixed culture of SVZ/RMS tissue, the cells were replated three times at 3–4 day intervals, then incubated with shaking for 20 min before use.

Coculture of SVZ/RMS Astrocytes with Slit-Expressing Cells

Stably transfected HEK cell lines expressing the full-length *Xenopus* Slit protein, and control HEK cells transfected with the vector plasmid (**Wu et al., 1999**) were mixed with 2% collagen gel and plated as one 10 μl gel-cell aggregate in each well of 24-well plates. Following a 1 hr incubation to polymerize the cell-containing gel, the gel pieces were cultured with DMEM medium containing 2% FBS and 50 U/ml penicillin-streptomycin overnight. Cultured SVZ/RMS astrocytes were resuspended in the same medium, plated into the same dish as the gel piece, and cultured at 37°C in a 5% CO_2 incubator. Seventy hours later, the cells were fixed with 4% PFA in 0.1 M phosphate buffer and immunostained with an anti-GFAP antibody. The distribution of GFAP+ cells on the gel pieces (within 500 μm of the edge) containing Slit-expressing cells and control cells were compared as follows: the merged images of nine optical Z-sections of the area at 5 μm intervals were obtained by confocal laser microscopy (10× dry objective lens, LSM5 PASCAL, Zeiss). The area that was GFAP+ in the 500 μm wide strip just inside the edge of the gel piece was determined using NIH ImageJ software.

Transfection of a Dominant-Negative Form of Robo

Cultured astrocytes were transfected with a plasmid encoding either a GFP-tagged dominant-negative form of Robo1 (Robo DN) or GFP (control) using Lipofectamine LTX Plus reagent (Invitrogen), three times at 12 hr intervals. Twelve hours after the final transfection, the cells were plated as described above, and then cultured for 60 hr before fixation.

Migration of New Neurons Associated with Cultured SVZ/RMS Astrocytes

The SVZ was dissected from P0-2 WT and *S1*$^{-/-}$ mice, the cells were dissociated and reaggregated, and the aggregates were cut into pieces (150–200 μm in diameter), as described above. The pieces of WT and *S1*$^{-/-}$ cells were plated on laminin-coated dishes or on monolayer cultures of SVZ/RMS astrocytes transfected with Robo DN or control vector (GFP), from WT or *Gfap-EGFP* mice and cultured for 24–36 hr, before imaging. The migration behavior of new neurons and their interaction with astrocytes were recorded by time-lapse imaging at 6 or 8 min intervals for 3–5 hr using confocal microscopy. The tracks of continuously migrating cells with the typical morphology of new neurons that could be traced for more than 40 min were used to calculate the migration speed in each situation.

To observe the furrow formation on astrocytes in 3D culture, the aggregates of SVZ cells dissociated from *Dcx-DsRed* mice were embedded into Matrigel in which SVZ/RMS astrocytes from *Gfap-EGFP* mice were suspended. After 24 hr of culture, time-lapse images were automatically captured by a confocal laser microscope (LSM710, Zeiss), every 2 min as 20 optical Z sections (Z-steps: 1 μm), for 3 hr.

Statistical Analysis

All data were expressed as the mean ± standard error of the mean (SEM). Differences between means were determined by two-tailed Student's t test or one-way ANOVA followed by a Tukey-Kramer multiple comparison test. A p value of <0.05 was considered significant.

SUPPLEMENTAL INFORMATION

Supplemental Information includes four figures, five movies, and Supplemental Experimental Procedures and can be found with this article online at **doi:10.1016/j.neuron.2010.06.018**.

ACKNOWLEDGMENTS

We thank the anonymous reviewers for helpful comments on the manuscript; Dr. Fujio Murakami for providing the specific antibodies to Robo1 and Robo2; Dr. Didier Trono for providing the lentivirus packaging plasmids, psPAX2 and pMD2.G; Dr. Nathaniel Heintz and the Mutant Mouse Regional Resource Center (MMRRC) for providing the Gfap-EGFP mice; and Drs. Ichiro Miyoshi, Tatsumi Hirata, Francois Renault-Mihara and Takehiko Sunabori and Miss Rie Ueda for technical support. This work was supported by research grants from the Ministry of Education, Culture, Sports, Science & Technology (MEXT), Ministry of Health, Labor and Welfare (MHLW), Japan Society for the Promotion of Science (JSPS), Human Frontier Science Program (HFSP), Toray Science Foundation, Keio University Medical Science Fund, Inoue Foundation for Science, NOVARTIS Foundation (Japan) for the Promotion of Science, and Kowa Life Science Foundation. J.Y.W is supported by NIH (CA114197, CA107193) and James S. McDonnell Foundation. N.K. was an Inoue Fellow.

Accepted: June 8, 2010
Published: July 28, 2010

REFERENCES

Andrews, W., Liapi, A., Plachez, C., Camurri, L., Zhang, J., Mori, S., Murakami, F., Parnavelas, J.G., Sundaresan, V., and Richards, L.J. (2006). Robo1 regulates the development of major axon tracts and interneuron migration in the forebrain. Development *133*, 2243–2252.

Andrews, W.D., Barber, M., and Parnavelas, J.G. (2007). Slit-Robo interactions during cortical development. J. Anat. *211*, 188–198.

Anton, E.S., Marchionni, M.A., Lee, K.F., and Rakic, P. (1997). Role of GGF/neuregulin signaling in interactions between migrating neurons and radial glia in the developing cerebral cortex. Development *124*, 3501–3510.

Anton, E.S., Ghashghaei, H.T., Weber, J.L., McCann, C., Fischer, T.M., Cheung, I.D., Gassmann, M., Messing, A., Klein, R., Schwab, M.H., et al. (2004). Receptor tyrosine kinase ErbB4 modulates neuroblast migration and placement in the adult forebrain. Nat. Neurosci. *7*, 1319–1328.

Belvindrah, R., Hankel, S., Walker, J., Patton, B.L., and Müller, U. (2007). Beta1 integrins control the formation of cell chains in the adult rostral migratory stream. J. Neurosci. *27*, 2704–2717.

Bolteus, A.J., and Bordey, A. (2004). GABA release and uptake regulate neuronal precursor migration in the postnatal subventricular zone. J. Neurosci. *24*, 7623–7631.

Brose, K., Bland, K.S., Wang, K.H., Arnott, D., Henzel, W., Goodman, C.S., Tessier-Lavigne, M., and Kidd, T. (1999). Slit proteins bind Robo receptors and have an evolutionarily conserved role in repulsive axon guidance. Cell *96*, 795–806.

Chazal, G., Durbec, P., Jankovski, A., Rougon, G., and Cremer, H. (2000). Consequences of neural cell adhesion molecule deficiency on cell migration in the rostral migratory stream of the mouse. J. Neurosci. *20*, 1446–1457.

Doetsch, F., and Alvarez-Buylla, A. (1996). Network of tangential pathways for neuronal migration in adult mammalian brain. Proc. Natl. Acad. Sci. USA *93*, 14895–14900.

Doetsch, F., García-Verdugo, J.M., and Alvarez-Buylla, A. (1997). Cellular composition and three-dimensional organization of the subventricular germinal zone in the adult mammalian brain. J. Neurosci. *17*, 5046–5061.

Fields-Berry, S.C., Halliday, A.L., and Cepko, C.L. (1992). A recombinant retrovirus encoding alkaline phosphatase confirms clonal boundary assignment in lineage analysis of murine retina. Proc. Natl. Acad. Sci. USA *89*, 693–697.

Garcia-Marques, J., De Carlos, J.A., Greer, C.A., and Lopez-Mascaraque, L. (2009). Different astroglia permissivity controls the migration of olfactory bulb interneuron precursors. Glia *58*, 218–230.

Ghashghaei, H.T., Weber, J., Pevny, L., Schmid, R., Schwab, M.H., Lloyd, K.C., Eisenstat, D.D., Lai, C., and Anton, E.S. (2006). The role of neuregulin-ErbB4 interactions on the proliferation and organization of cells in the subventricular zone. Proc. Natl. Acad. Sci. USA *103*, 1930–1935.

Hammond, R., Vivancos, V., Naeem, A., Chilton, J., Mambetisaeva, E., Mambitisaeva, E., Andrews, W., Sundaresan, V., and Guthrie, S. (2005). Slit-mediated repulsion is a key regulator of motor axon pathfinding in the hindbrain. Development *132*, 4483–4495.

Hatten, M.E. (2002). New directions in neuronal migration. Science *297*, 1660–1663.

Hirota, Y., Ohshima, T., Kaneko, N., Ikeda, M., Iwasato, T., Kulkarni, A.B., Mikoshiba, K., Okano, H., and Sawamoto, K. (2007). Cyclin-dependent kinase 5 is required for control of neuroblast migration in the postnatal subventricular zone. J. Neurosci. *27*, 12829–12838.

Hu, H. (1999). Chemorepulsion of neuronal migration by Slit2 in the developing mammalian forebrain. Neuron *23*, 703–711.

Hu, H., and Rutishauser, U. (1996). A septum-derived chemorepulsive factor for migrating olfactory interneuron precursors. Neuron *16*, 933–940.

Jankovski, A., and Sotelo, C. (1996). Subventricular zone-olfactory bulb migratory pathway in the adult mouse: cellular composition and specificity as determined by heterochronic and heterotopic transplantation. J. Comp. Neurol. *371*, 376–396.

Kaneko, N., and Sawamoto, K. (2009). Adult neurogenesis and its alteration under pathological conditions. Neurosci. Res. *63*, 155–164.

Lois, C., and Alvarez-Buylla, A. (1994). Long-distance neuronal migration in the adult mammalian brain. Science *264*, 1145–1148.

Lois, C., García-Verdugo, J.M., and Alvarez-Buylla, A. (1996). Chain migration of neuronal precursors. Science *271*, 978–981.

Long, J.E., Garel, S., Alvarez-Dolado, M., Yoshikawa, K., Osumi, N., Alvarez-Buylla, A., and Rubenstein, J.L. (2007). Dlx-dependent and -independent regulation of olfactory bulb interneuron differentiation. J. Neurosci. *27*, 3230–3243.

Marín, O., and Rubenstein, J.L. (2003). Cell migration in the forebrain. Annu. Rev. Neurosci. *26*, 441–483.

Marín, O., Plump, A.S., Flames, N., Sánchez-Camacho, C., Tessier-Lavigne, M., and Rubenstein, J.L. (2003). Directional guidance of interneuron migration to the cerebral cortex relies on subcortical Slit1/2-independent repulsion and cortical attraction. Development *130*, 1889–1901.

Mason, H.A., Ito, S., and Corfas, G. (2001). Extracellular signals that regulate the tangential migration of olfactory bulb neuronal precursors: inducers, inhibitors, and repellents. J. Neurosci. *21*, 7654–7663.

Miyata, T., Kawaguchi, A., Okano, H., and Ogawa, M. (2001). Asymmetric inheritance of radial glial fibers by cortical neurons. Neuron *31*, 727–741.

Murase, S., and Horwitz, A.F. (2002). Deleted in colorectal carcinoma and differentially expressed integrins mediate the directional migration of neural precursors in the rostral migratory stream. J. Neurosci. *22*, 3568–3579.

Nguyen Ba-Charvet, K.T., Brose, K., Marillat, V., Kidd, T., Goodman, C.S., Tessier-Lavigne, M., Sotelo, C., and Chédotal, A. (1999). Slit2-Mediated chemorepulsion and collapse of developing forebrain axons. Neuron *22*, 463–473.

Nguyen-Ba-Charvet, K.T., Picard-Riera, N., Tessier-Lavigne, M., Baron-Van Evercooren, A., Sotelo, C., and Chédotal, A. (2004). Multiple roles for slits in the control of cell migration in the rostral migratory stream. J. Neurosci. *24*, 1497–1506.

Okano, H., and Sawamoto, K. (2008). Neural stem cells: involvement in adult neurogenesis and CNS repair. Philos. Trans. R. Soc. Lond. B Biol. Sci. *363*, 2111–2122.

Petreanu, L., and Alvarez-Buylla, A. (2002). Maturation and death of adult-born olfactory bulb granule neurons: role of olfaction. J. Neurosci. *22*, 6106–6113.

Plump, A.S., Erskine, L., Sabatier, C., Brose, K., Epstein, C.J., Goodman, C.S., Mason, C.A., and Tessier-Lavigne, M. (2002). Slit1 and Slit2 cooperate to prevent premature midline crossing of retinal axons in the mouse visual system. Neuron *33*, 219–232.

Rakic, P. (1971). Guidance of neurons migrating to the fetal monkey neocortex. Brain Res. *33*, 471–476.

Rakic, P. (1972). Mode of cell migration to the superficial layers of fetal monkey neocortex. J. Comp. Neurol. *145*, 61–83.

Sawamoto, K., Wichterle, H., Gonzalez-Perez, O., Cholfin, J.A., Yamada, M., Spassky, N., Murcia, N.S., Garcia-Verdugo, J.M., Marin, O., Rubenstein, J.L., et al. (2006). New neurons follow the flow of cerebrospinal fluid in the adult brain. Science *311*, 629–632.

Schmid, R.S., McGrath, B., Berechid, B.E., Boyles, B., Marchionni, M., Sestan, N., and Anton, E.S. (2003). Neuregulin 1-erbB2 signaling is required for the establishment of radial glia and their transformation into astrocytes in cerebral cortex. Proc. Natl. Acad. Sci. USA *100*, 4251–4256.

Shiau, C.E., Lwigale, P.Y., Das, R.M., Wilson, S.A., and Bronner-Fraser, M. (2008). Robo2-Slit1 dependent cell-cell interactions mediate assembly of the trigeminal ganglion. Nat. Neurosci. *11*, 269–276.

Snapyan, M., Lemasson, M., Brill, M.S., Blais, M., Massouh, M., Ninkovic, J., Gravel, C., Berthod, F., Götz, M., Barker, P.A., et al. (2009). Vasculature guides migrating neuronal precursors in the adult mammalian forebrain via brain-derived neurotrophic factor signaling. J. Neurosci. *29*, 4172–4188.

Suzuki, S.O., and Goldman, J.E. (2003). Multiple cell populations in the early postnatal subventricular zone take distinct migratory pathways: a dynamic study of glial and neuronal progenitor migration. J. Neurosci. *23*, 4240–4250.

Tamada, A., Kumada, T., Zhu, Y., Matsumoto, T., Hatanaka, Y., Muguruma, K., Chen, Z., Tanabe, Y., Torigoe, M., Yamauchi, K., et al. (2008). Crucial roles of Robo proteins in midline crossing of cerebellofugal axons and lack of their up-regulation after midline crossing. Neural Dev. *3*, 29.

Uchiyama, Y., and Watanabe, M. (1984). A morphometric study of developing pancreatic acinar cells of rats during prenatal life. Cell Tissue Res. *237*, 117–122.

Wang, X., Qiu, R., Tsark, W., and Lu, Q. (2007). Rapid promoter analysis in developing mouse brain and genetic labeling of young neurons by doublecortin-DsRed-express. J. Neurosci. Res. *85*, 3567–3573.

Wichterle, H., Garcia-Verdugo, J.M., and Alvarez-Buylla, A. (1997). Direct evidence for homotypic, glia-independent neuronal migration. Neuron *18*, 779–791.

Wu, W., Wong, K., Chen, J., Jiang, Z., Dupuis, S., Wu, J.Y., and Rao, Y. (1999). Directional guidance of neuronal migration in the olfactory system by the protein Slit. Nature *400*, 331–336.

Zheng, C., Heintz, N., and Hatten, M.E. (1996). CNS gene encoding astrotactin, which supports neuronal migration along glial fibers. Science *272*, 417–419.

Neuron

Neural RNA-Binding Protein Musashi1 Controls Midline Crossing of Precerebellar Neurons through Posttranscriptional Regulation of Robo3/Rig-1 Expression

Ken-ichiro Kuwako,[1,2,*] Kyoko Kakumoto,[1] Takao Imai,[1] Mana Igarashi,[1] Takao Hamakubo,[3] Shin-ichi Sakakibara,[4] Marc Tessier-Lavigne,[5] Hirotaka James Okano,[1] and Hideyuki Okano[1,*]

[1]Department of Physiology

[2]Bridgestone Laboratory of Developmental and Regenerative Neurobiology

Keio University School of Medicine, 35 Shinanomachi, Shinjuku-ku, Tokyo 160-8582, Japan

[3]The Research Center for Advanced Science and Technology, The University of Tokyo 4-6-1 Komaba, Meguro-ku, Tokyo 153-8904, Japan

[4]Laboratory of Molecular Neurobiology, Faculty of Human Sciences, Waseda University, 2-579-15 Mikazima Tokorozawa, Saitama 359-1192, Japan

[5]Division of Research, Genentech Inc., 1 DNA way, South San Francisco, CA 94080, USA

*Correspondence: kuwako@sc.itc.keio.ac.jp (K.-i.K.), hidokano@sc.itc.keio.ac.jp (H.O.)

DOI 10.1016/j.neuron.2010.07.005

SUMMARY

Precisely regulated spatiotemporal gene expression is essential for the establishment of neural circuits. In contrast to the increasing evidence for transcriptional regulation of axon guidance cues and receptors, the role of posttranscriptional regulation in axon guidance, especially in vivo, remains poorly characterized. Here, we demonstrate that the expression of Slit receptor Robo3/Rig-1, which plays crucial roles in axonal midline crossing, is regulated by a neural RNA-binding protein Musashi1 (Msi1). Msi1 binds to *Robo3* mRNA through RNA recognition motifs and increases the protein level of Robo3 without affecting its mRNA level. In *Msi1*-deficient precerebellar neurons, Robo3 protein, but not its mRNA, is dramatically reduced. Moreover, similar to defects in *Robo3*-deficient mice, axonal midline crossing and neuronal migration of precerebellar neurons are severely impaired in *Msi1*-deficient mice. Together, these findings indicate that Msi1-mediated posttranscriptional regulation of Robo3 controls midline crossing of precerebellar neurons.

INTRODUCTION

During development, growing axons travel toward their final destinations through long and complicated routes. Axons pass through several intermediate targets sequentially to reach their far-distant destinations, so that a series of short segments divided by intermediate targets makes up an entire trajectory (Tessier-Lavigne and Goodman, 1996). For instance, certain axons are attracted to the floor plate, a prototypical intermediate target, cross the midline at the floor plate, and then move on toward their next target.

As excellent models for understanding the regulatory mechanisms of midline crossing, the axonal projections and neuronal migration of hindbrain precerebellar neurons have been studied in great detail. The axons of precerebellar neurons, the so-called climbing fiber and mossy fiber, are the two main afferent networks conveying information to the cerebellar cortex. The germinative neuroepithelium located at the most dorsal part of the caudal hindbrain, the rhombic lip, gives rise to all precerebellar neurons including inferior olivary (IO) neurons, lateral reticular nucleus (LRN) neurons, external cuneate nucleus (ECN) neurons and pontine nucleus (PN) neurons at different developmental stages (IO neurons: E10–11, LRN/ECN neurons: E11–12, PN neurons: E12–16; Pierce, 1966; Altman and Bayer, 1987a; Bourrat and Sotelo, 1988, 1991). These cells then migrate toward the ventral midline with a leading process that initiates the tangential migratory pathway (Bourrat and Sotelo, 1988). Although the leading processes, which correspond to the future axons, of all precerebellar neurons cross the ventral midline at the floor plate, their cell bodies show distinct behaviors around the floor plate. IO neurons with a very long leading process migrate toward the midline, and their processes cross the midline first but the cell bodies stop just before crossing the midline; thus, IO neurons project their axons across the floor plate into the contralateral cerebellum (Figure 1A; Altman and Bayer, 1987b; Marillat et al., 2004). On the other hand, LRN/ECN neurons with a short process migrate toward the midline, and both the processes and the cell bodies cross the ventral midline almost simultaneously, thus LRN/ECN neurons project their axons into the ipsilateral cerebellum (Figure 1A; Marillat et al., 2004).

The classical guidance cues secreted from floor plate cells, such as Netrin and Slit, play major roles in the midline crossing of hindbrain precerebellar neurons. Netrin-1 attracts all precerebellar neurons through its receptor "deleted in colorectal cancer" (DCC) (Yee et al., 1999; Bloch-Gallego et al., 1999; Alcántara et al., 2000; de Diego et al., 2002; Taniguchi et al., 2002). Members of the Slit family (Slit1, Slit2, Slit3) and their receptors of the Robo family (Robo1, Robo2, Robo3/Rig-1 [hereafter referred to as Robo3]) are expressed

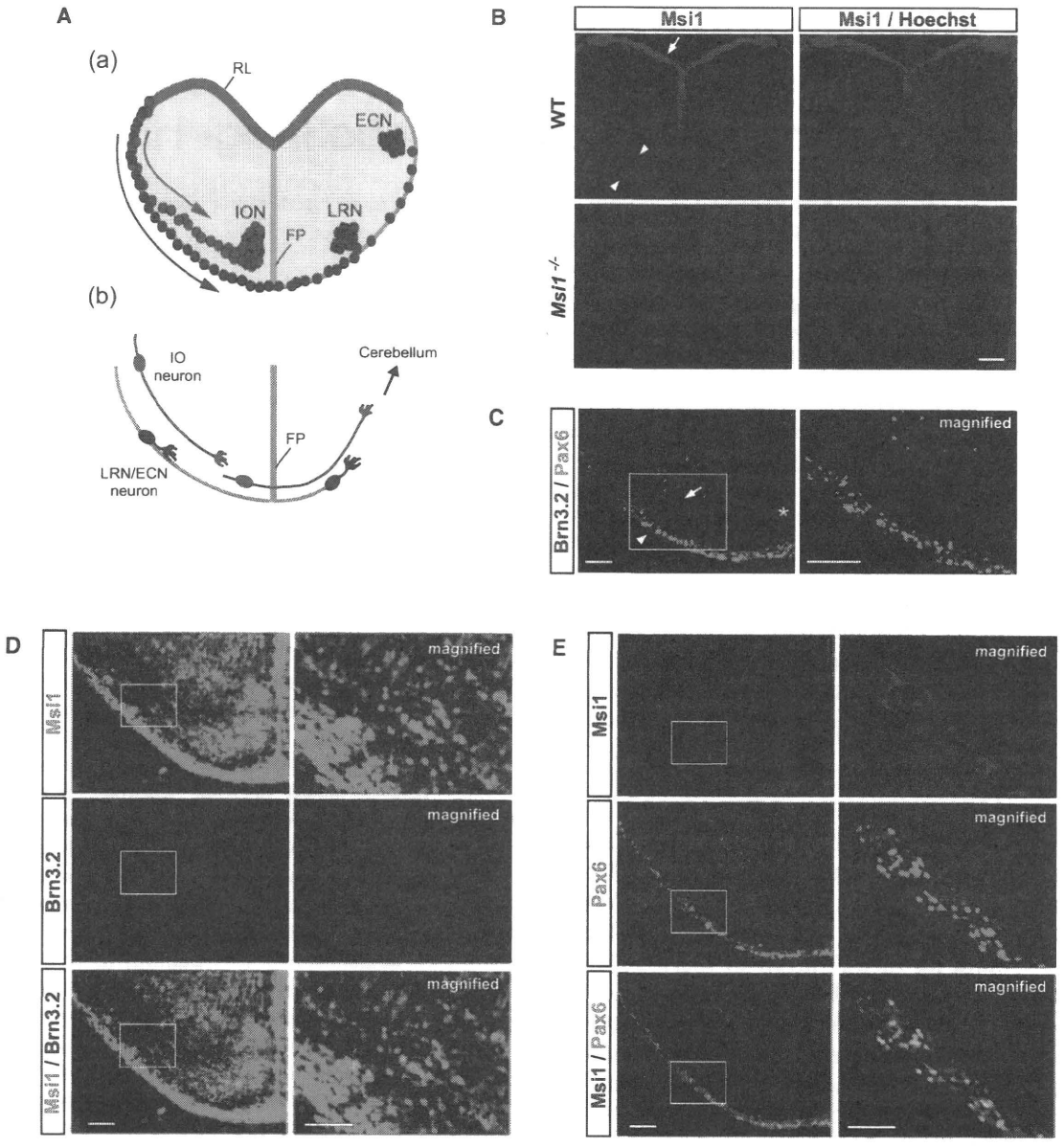

Figure 1. Msi1 Is Expressed in Migrating Precerebellar Neurons

(A) Schematic representations of the migratory pathways (a) and the axonal midline crossing (b) of IO and LRN/ECN neurons in cross sections of the embryonic hindbrain. Precerebellar neurons originate from the rhombic lip (RL) and migrate dorsoventrally toward the floor plate (FP). LRN/ECN neurons (blue circles in (a)) migrate superficially in the marginal stream and both axons and cell bodies cross the floor plate. IO neurons (red circles in (a)) migrate along a deeper pathway in the submarginal stream. The axons of IO neurons cross the floor plate, while the cell bodies do not cross the floor plate and form the inferior olivary nucleus (ION) just adjacent to the midline.

(B–E) Immunohistochemistry on coronal sections of E13.5 hindbrain from wild-type (WT) or *Msi1*-deficient (*Msi1*$^{-/-}$) mice. (B) Expression of Msi1. Msi1 was widely expressed in the hindbrain including the rhombic lip (arrow) and the migratory streams of precerebellar neurons (arrowheads). (C) IO (arrow) and LRN/ECN (arrowhead) neurons in WT mice were immunolabeled with antibodies against Brn3.2 and Pax6, respectively. The asterisk indicates the floor plate. The box in the left panel indicates the position of the high-magnification image in the right panel. (D and E) Sections of E13.5 hindbrain from WT mice were coimmunostained with anti-Msi1 and anti-Brn3.2 antibodies (D), or anti-Msi1 and anti-Pax6 antibodies (E). The boxes in the left panels indicate the positions of the high-magnification images shown in the right panels. Note that all migrating IO and LRN/ECN neurons express Msi1.

Scale bar: (B) 200 μm; (C) 100 μm; (D and E) left panels 100 μm, right panels 50 μm (see also Figure S1).

in the developing hindbrain and also contribute significantly to midline crossing of precerebellar neurons (Marillat et al., 2004; Di Meglio et al., 2008).

The expression levels of axon guidance receptors on the growing axon are a crucial determinant of axonal attraction and repulsion (Dickson and Gilestro, 2006). In spinal cord

commissural axons, the expression levels of several surface proteins, including L1, TAG1 and the guidance receptors EphA2, Robo1, and Robo3, are dramatically changed at the midline (Dodd et al., 1988; Brittis et al., 2002; Sabatier et al., 2004). While many transcription factors regulating the expressions of guidance receptors have been identified, for instance Pax-2 and Lhx2/Lhx9 for Robo3 (Yuan et al., 2002; Wilson et al., 2008), the contribution of posttranscriptional regulation remains largely unknown.

Robo3 has a crucial role in axonal midline crossing in both the hindbrain and the spinal cord. The defects in *Robo3*-deficient (*Robo3*$^{-/-}$) mice indicate that Robo3 interferes with Slit-mediated repulsive signal(s) (Sabatier et al., 2004). In the hindbrain, the axons of *Robo3*$^{-/-}$ precerebellar neurons fail to cross the floor plate and project to the ipsilateral cerebellum (Marillat et al., 2004). Moreover, many mutations in the human *Robo3* gene have been identified in individuals with the autosomal-recessive syndrome of horizontal gaze palsy with progressive scoliosis (HGPPS) (Jen et al., 2004). HGPPS patients have multiple defects, including aberrant ipsilateral projections of ascending and descending fibers in the hindbrain (Jen, 2008), that are quite consistent with the defects in *Robo3*$^{-/-}$ mice

The Musashi family is an evolutionarily conserved family of RNA-binding proteins that regulate the translation of target mRNAs. In mammals, this family comprised of two members, Musashi1 (Msi1) and Musashi2 (Msi2). Both Msi1 and Msi2 are predominantly expressed in neural stem/progenitor cells and are thought to be involved in the regulation of stem cell self-renewal by controlling the translation of target mRNAs (Sakakibara et al., 1996, 2001, 2002). To date, two target mRNAs of Msi1, the Notch signaling inhibitor *m-numb* and the cell cycle inhibitor *p21*^{WAF}, have been identified. Msi1 represses the translations of *m-numb* and *p21*^{WAF} through sequence specific binding to the 3′UTR (3′untranslated region) of mRNAs (Imai et al., 2001; Battelli et al., 2006). On the other hand, during *Xenopus* oocyte maturation, the *Xenopus* homolog of Msi1 NRP promotes the translation of multiple mRNAs through binding to their 3′UTRs (Charlesworth et al., 2006). Thus, Msi1 can potentially function as both a translational activator and a repressor, depending on the cellular content and target mRNA.

In this study, we found that Msi1 was also expressed in developing postmitotic neurons. Using *Msi1*-deficient (*Msi1*$^{-/-}$) mice, we demonstrated that Msi1 was required for axonal midline crossing and neuronal migration of IO and LRN/ECN neurons. We also showed that Msi1 controlled Robo3 expression at the posttranscriptional level in vitro and in vivo. Furthermore, we showed that the expression level of Robo3 controlled by Msi1 determined the midline crossing of precerebellar neurons. These findings reveal a critical role for posttranscriptional regulation of the axon guidance machinery via specific RNA binding proteins.

RESULTS

Msi1 Is Expressed in Developing Precerebellar Neurons

To explore novel functions of Msi1, we first examined the detailed expression pattern of Msi1 in the developing nervous system. As we previously reported (Kaneko et al., 2000), Msi1 was highly expressed in regions where neural stem/progenitor cells reside (see Figure S1A available online). By comparing the expression patterns in wild-type (WT) and *Msi1*$^{-/-}$ mice, however, we also found that Msi1 was expressed in developing neurons in various regions including the hindbrain, spinal cord and cerebral cortex (Figure S1A). In the hindbrain, for example, Msi1 was highly expressed in postmitotic neurons in addition to neural stem/progenitor cells, at least from E12.5 to E18.5 (Figure S1B). To investigate the functions of Msi1 in developing neurons, we focused on precerebellar neurons in the hindbrain. At E13.5 when IO and LRN/ECN neurons are migrating in the submarginal and marginal streams, respectively, from the rhombic lip toward the ventral midline (Figure 1A), Msi1 was expressed in the entire region of the caudal hindbrain including the migratory streams of precerebellar neurons and the rhombic lip (Figure 1B). Msi2, in contrast, was not expressed in the migratory streams of precerebellar neurons (Figure S1C). As shown in Figures 1D and 1E, coimmunostaining experiments confirmed that Msi1 was expressed in all migrating IO and LRN/ECN neurons which were specifically labeled with antibodies against Brn3.2 and Pax6, respectively (Di Meglio et al., 2008; Figure 1C). Further immunohistochemical analysis for Msi1 expression under conditions in which the fluorescence signal was not saturated revealed that the expression levels of Msi1 apparently decreased in both IO and LRN/ECN neurons as they approached the floor plate (Figure S1D), suggesting that Msi1 expression might be spatially and temporally regulated in precerebellar neurons during their migration.

Msi1 Is Essential for Midline Crossing of IO and LRN/ECN Neurons

To explore the possibility that Msi1 regulates axonal projections and migration of precerebellar neurons, we next examined whether midline crossing of precerebellar neurons is disrupted in *Msi1*$^{-/-}$ mice. We first analyzed midline crossing of IO neurons. The unilateral injection of DiI crystals into the cerebellum in P0 mice (Figure 2A) revealed that the retrogradely DiI-labeled inferior olivary nucleus was located on the side contralateral to the injection side and that DiI-labeled IO axons crossed the floor plate in all WT (n = 18 of 18) and *Msi1* heterozygous mice (n = 16 of 16) (Figure 2B). In *Msi1*$^{-/-}$ mice, however, the DiI-labeled inferior olivary nucleus was abnormally located ipsilateral (n = 14 of 19) or both contralateral and ipsilateral (n = 5 of 19) to the injection side (Figure 2B). Moreover, in *Msi1*$^{-/-}$ mice in which the DiI-labeled inferior olivary nucleus was only located ipsilateral to the injection side, DiI-labeled IO axons were never observed in the floor plate (Figure 2B). These results suggest that IO axons abnormally project to the ipsilateral cerebellum without crossing the floor plate in *Msi1*$^{-/-}$ mice. We next attempted to clarify whether the ipsilateral projection of IO axons in *Msi1*$^{-/-}$ mice resulted from a failure of axonal midline crossing (axons and cell bodies do not cross the floor plate) or an abnormal midline crossing of the cell bodies of IO neurons (axons and cell bodies both cross the floor plate). To distinguish these possibilities, we investigated the crossing of IO axons at E13.5, a peak time for midline crossing of IO neurons in WT mice (Figure 2C). Since EphA4, a receptor tyrosine kinase, is specifically expressed in IO neurons but not in LRN/ECN neurons at E13.5 (de Diego et al., 2002; Figure 4C), we labeled

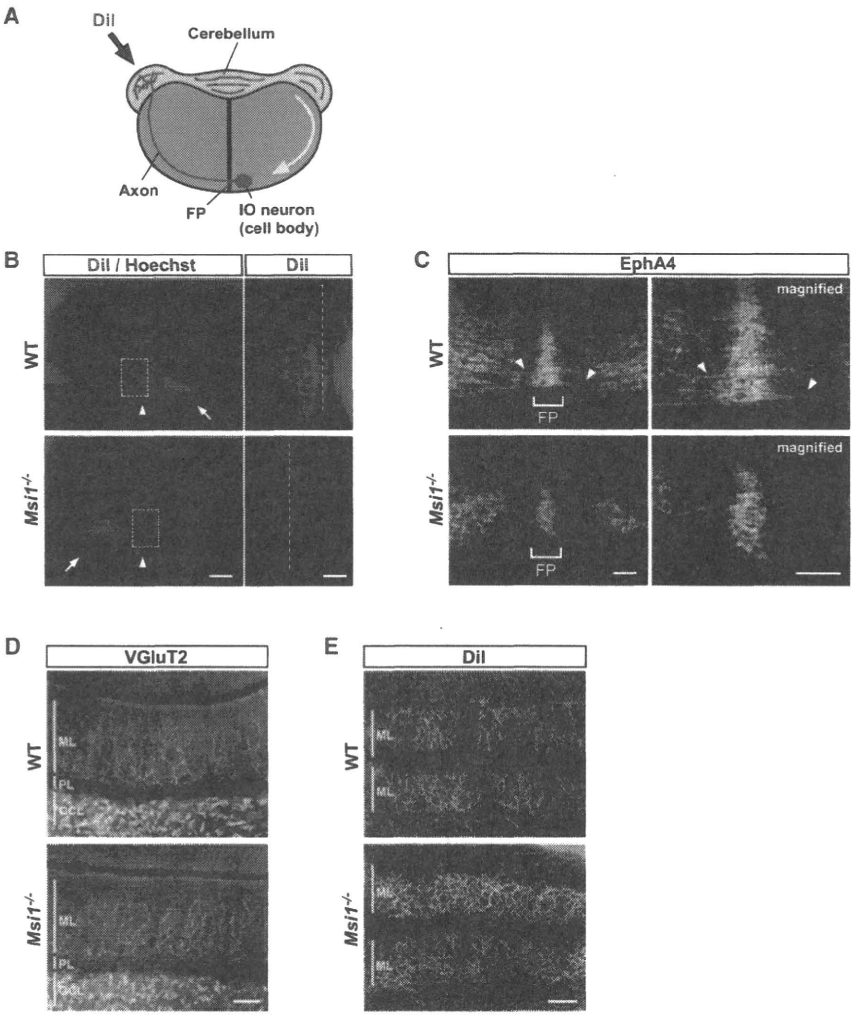

Figure 2. Axons of IO Neurons Do Not Cross the Midline in *Msi1*-Deficient Mice

(A) Schematic representation of a unilateral DiI injection into the cerebellum. The yellow arrow shows the migratory pathway of the IO neurons illustrated in the scheme. FP: floor plate.

(B) DiI crystals were unilaterally injected into the P0 mice cerebellum. IO neurons in wild-type (WT) mice were retrogradely labeled only contralateral to the injection site (arrow in left-top panel), whereas in *Msi1*-deficient (*Msi1*$^{-/-}$) mice IO neurons were labeled ipsilateral to the injection side (arrow in left-bottom panel). The arrowheads in the left panels indicate the midline. The dotted boxes in the left panels indicate the positions of the high-magnification images shown in the right panels. The dashed lines in the right panels represent the midline.

(C) Immunolabeling of IO axons crossing the floor plate. Coronal sections of E13.5 hindbrain were immunostained with anti-EphA4 antibody. The right panels show magnified views of the left panels. Many IO axons were labeled around the floor plate (arrowheads) in WT mice, while only a few IO axons were detected around the floor plate in *Msi1*$^{-/-}$ mice. Some non-specific signals were detected in the floor plate, which were distinguishable from IO axons by morphology. FP: floor plate.

(D and E) Sagittal sections from 6-week-old mice cerebellum. (D) Sections were immunostained with anti-VGluT2 antibody for the labeling of axon terminals of IO neurons. (E) DiI crystals were injected into the inferior olivary nucleus at 6 weeks of age for the anterograde labeling of IO axons. In both WT and *Msi1*$^{-/-}$ mice, axons of IO neurons projected into the cerebellum. ML: molecular layer, PL: Purkinje cell layer, GCL: granule cell layer.

Scale bar: (B) left panels 200 μm, right panels 50 μm; (C) 50 μm; (D) 50 μm; (E) 100 μm.

the crossing IO axons using an anti-EphA4 antibody. At this stage, the expression level of EphA4 was not apparently altered in the submarginal stream in E13.5 *Msi1*$^{-/-}$ mice (Figure 4C), suggesting that a deficiency of Msi1 is unlikely to reduce EphA4 expression. Around the floor plate, only a few IO axons were detected in *Msi1*$^{-/-}$ mice, while many EphA4-positive IO axons were detected in WT mice (Figure 2C), indicating that IO axons have difficulty crossing the floor plate in *Msi1*$^{-/-}$ mice. Furthermore, like WT mice, either Brn3.2-positive or Hoechst-stained cells were never observed in the floor plate at the level of the inferior olivary nucleus in *Msi1*$^{-/-}$ mice at least from E12.5 to E18.5 (data not shown), suggesting that IO neurons do not cross the floor plate in these mice. Taken together, our results suggest that in *Msi1*$^{-/-}$ mice, the axons do not cross the floor plate, while the cell bodies appropriately stop adjacent to the floor plate, explaining why the axons project to the ipsilateral cerebellum. We further examined the projection patterns of IO axons in the cerebellum. In 6-week-old *Msi1*$^{-/-}$ mice, the number and distribution patterns of vesicular glutamate transporter 2 (VGluT2)-positive puncta, which is selectively localized in synaptic vesicles in the terminals of IO axons in the molecular layer, appeared to be essentially normal when compared to those of WT mice (Figure 2D). The anterograde-DiI tracing of IO axons from the inferior olivary nucleus also revealed that the axonal density and terminal axonal branching of IO neurons in the molecular layer were normal in 6-week-old *Msi1*$^{-/-}$ mice (Figure 2E). These results suggest that IO axons in *Msi1*$^{-/-}$ mice, which have failed to cross the midline, still project to their appropriate target regions in the cerebellum, but on the ipsilateral rather than the contralateral side.

We next analyzed midline crossing of LRN/ECN neurons. By whole mount immunostaining for Pax6, LRN/ECN neurons migrating on the surface of the E13.5 hindbrain were clearly visualized in both WT and *Msi1*$^{-/-}$ mice (Figure 3A). In the lateral hindbrain, the trajectory and the number of migrating LRN/ECN neurons in *Msi1*$^{-/-}$ mice appeared to be normal. In the ventral hindbrain, however, the number of migrating LRN/ECN neurons gradually decreased toward the ventral midline in *Msi1*$^{-/-}$ mice, whereas many LRN/ECN neurons were detected in the ventral midline area in WT mice. These results suggest that the absence

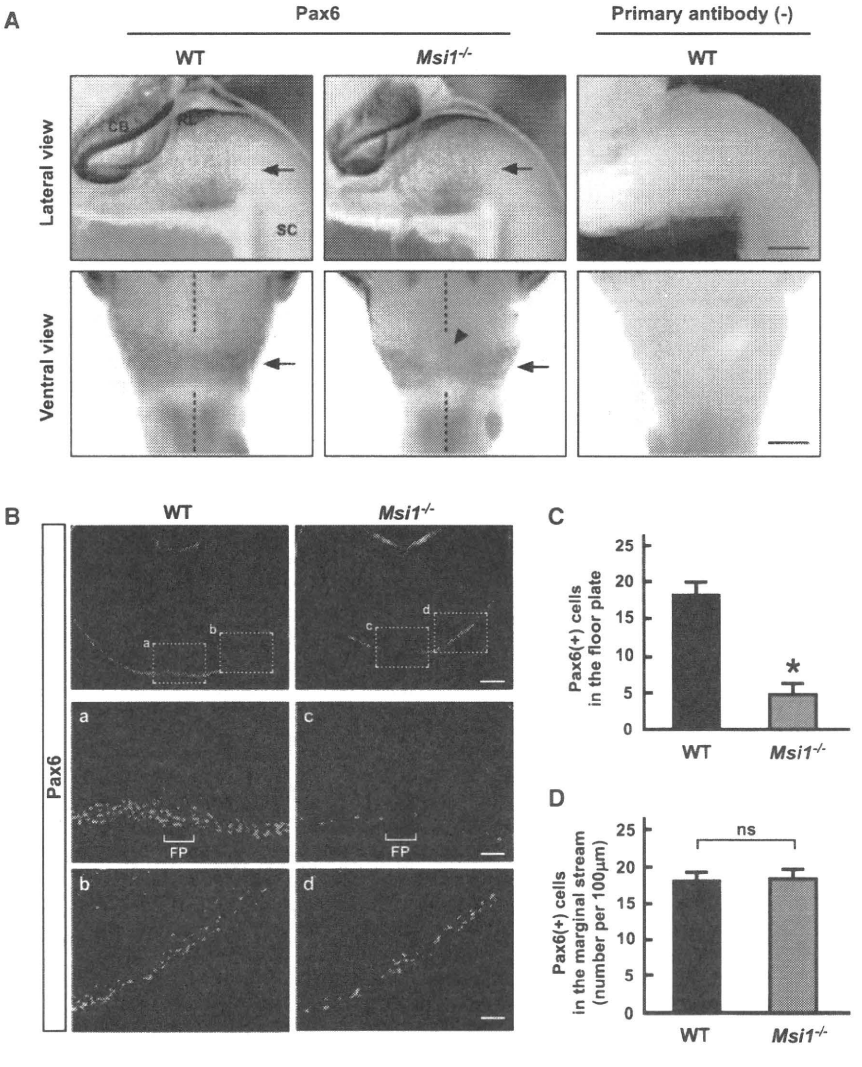

Figure 3. LRN/ECN Neurons Do Not Cross the Midline in *Msi1*-Deficient Mice

(A) E13.5 whole-mount hindbrain immunostained with anti-Pax6 antibody. Migrating LRN/ECN neurons (arrows) were detected on the surface of the lateral and ventral hindbrain in both wild-type (WT) and *Msi1*-deficient (*Msi1*$^{-/-}$) mice. Note that the number of migrating LRN/ECN neurons was decreased around the midline (arrowhead) in *Msi1*$^{-/-}$ mice. The dashed lines show the midline. RL: rhombic lip, CB: cerebellum, SC: spinal cord.

(B) Coronal sections of E13.5 hindbrain from WT and *Msi1*$^{-/-}$ mice were immunostained with anti-Pax6 antibody. FP: floor plate.

(C and D) Quantification of the number of Pax6-positive cells in the floor plate (C) and the marginal stream (D). The quantified regions are indicated in (B): (a) and (c) for the floor plate, (b) and (d) for the marginal stream. The data represent mean ± SEM of four mice from independent experiments. *$p < 0.001$, ns: not significant ($p > 0.05$) by unpaired Student's t test.

(E) DiI crystals were unilaterally injected into the P0 WT or *Msi1*$^{-/-}$ mice cerebellum as shown in Figure 2A.

(F) In situ hybridization for *Barhl1* in coronal sections of E18.5 hindbrain. The dotted boxes in the left panels indicate the positions of the high-magnification images shown in the right panels. The arrowheads in the right panels indicate the presumptive scattered ECN neurons. The asterisks indicate the midline. In *Msi1*$^{-/-}$ mice, both LRN and ECN neurons formed the nerve nucleus at the correct position, even though ECN neurons tended to be less condensed.

Scale bar: (A) 0.5 mm; (B) top panels 200 μm, middle and bottom panels 50 μm; (E) 0.5 mm; (F) left panels 0.5 mm, right panels 100 μm (see also Figure S2).

of Msi1 expression may impair midline crossing of LRN/ECN neurons without affecting their generation. To further confirm this, we also analyzed E13.5 hindbrain sections by immunostaining for Pax6. Consistent with the observations in whole mount preparations (Figure 3A), the numbers of LRN/ECN neurons migrating in the lateral hindbrain were comparable in WT and *Msi1*$^{-/-}$ mice, but the number in the floor plate was dramatically reduced in *Msi1*$^{-/-}$ mice (Figure 3B). Quantification of these results revealed a 73% reduction of LRN/ECN neurons in the floor plate in *Msi1*$^{-/-}$ mice (Figure 3C). These results are probably not attributable to a delay in the migration of LRN/ECN neurons, because similar defects were also observed in E14.5 *Msi1*$^{-/-}$ mice (Figures S2A–S2C). Thus, these results suggest that loss of Msi1 expression results in impaired midline crossing of LRN/ECN neurons.

We further asked whether LRN/ECN neurons were able to form the nerve nucleus in *Msi1*$^{-/-}$ mice. Unilateral DiI-tracing and in situ hybridization for *Barhl1*, a transcription factor highly expressed in LRN/ECN neurons (Li et al., 2004), revealed that the lateral reticular nucleus and the external cuneatus nucleus formed at their normal positions in E18.5–P0

the number of migrating LRN/ECN neurons in the marginal stream was not reduced in *Msi1*$^{-/-}$ mice (Figures 3B and 3D) and the immunoreactivity of EphA4, which is specifically expressed in IO neurons (de Diego et al., 2002), was comparable in WT and *Msi1*$^{-/-}$ mice (Figure 4C), the decreased immunoreactivity of Robo3 likely reflects a decrease in expression in both IO and LRN/ECN neurons. Indeed, Msi1 and Robo3 were coexpressed in migrating precerebellar neurons in WT mice (Figures S3A–S3C). The floor plate-derived classical guidance cues appear to be unaffected by loss of Msi1 expression, because *Netrin-1*, *Slit1*, *Slit2*, and *Slit3* were normally expressed in floor plate cells in E13.5 *Msi1*$^{-/-}$ mice (Figure S3F). A western blot analysis using extracts from E13.5 caudal hindbrain showed a 75% reduction in the level of Robo3 protein in *Msi1*$^{-/-}$ mice, while the level of DCC was unchanged (Figures 4D and 4E). Since, in E13.5 caudal hindbrain, Msi2 was only expressed in the neuroepithelium (Figure S1C) in which Robo3 was not expressed (Marillat et al., 2004), Robo3 expression was not altered in E13.5 *Msi2*-deficient hindbrain (Figure S3G). The two recently identified splicing variants of Robo3, Robo3.1 and Robo3.2, were expressed in the caudal hindbrain and were equally downregulated in *Msi1*$^{-/-}$ mice (Figures S3H–S3K), suggesting that Msi1 may regulate the expressions of both Robo3.1 and Robo3.2 in a similar fashion. Thus, in the following experiments in which Robo3 cDNA was transfected into the cultured cells, we used Robo3.1, which reportedly antagonizes Slit-induced repulsion in spinal commissural neurons (Chen et al., 2008). We next examined *Robo3* mRNA expression by in situ hybridization and reverse transcription-polymerase chain reaction (RT-PCR). Interestingly, the expression pattern and level of *Robo3* mRNA in E12.5-13.5 *Msi1*$^{-/-}$ hindbrain were quite similar to those in WT (Figures 4F and 4G). These results suggest that Robo3 expression was decreased by the disruption of posttranscriptional regulation in *Msi1*$^{-/-}$ precerebellar neurons.

Unlike precerebellar neurons, the expression level of Robo3 protein was not decreased in *Msi1*$^{-/-}$ commissural neurons (Figures S3L–S3N), whose axonal midline crossing was normal (Figure S2D), suggesting that the expression of Robo3 might be differently regulated in different types of cells.

Msi1 Increases Robo3 Expression through Posttranscriptional Regulation

Since Msi1 has been characterized as an mRNA translational regulator (Okano et al., 2002, 2005), the evidence that loss of Msi1 reduces Robo3 expression through posttranscriptional regulation prompted us to examine the possibility that Msi1 regulates the translation of *Robo3* mRNA. To address this issue, we first examined whether Msi1 protein is associated with *Robo3* mRNA in vivo by an RNA-protein binding assay combining affinity precipitation with RT-PCR (Figure 5A). An abundance of *Robo3* transcripts was detected in immunoprecipitates from hindbrain extracts of WT but not *Msi1*$^{-/-}$ mice and required reverse transcription. Further analysis using specific primers for *Robo3.1* and *Robo3.2* revealed that Msi1 binds to both splicing variants (Figure S4A). *GAPDH* transcripts were not detected (Figure 5A). These results suggest that Msi1 binds to *Robo3* mRNA in vivo either directly or indirectly.

We also tested the possibility that Msi1 interacts with Robo3 protein to regulate its expression level. A coimmunoprecipitation assay in cDNA-transfected COS-7 cells revealed that Msi1 coprecipitated with the neuronal RNA-binding protein HuC, as we previously observed (K.K., H.J.O., and H.O.; unpublished data), but not with Robo3 protein (Figures 5B and S4B). These results suggest that Msi1 does not form a complex with Robo3 protein. We next examined whether Msi1 affects the stability of Robo3 protein using cycloheximide (CHX), a protein synthesis inhibitor. The reduced level of Robo3 protein in CHX-treated COS-7 cells was not altered even in the presence of Msi1 (Figure 5C), suggesting that Msi1 is unlikely to control the level of Robo3 protein through protein stabilization.

To further examine Msi1-mediated regulation of Robo3 expression, we used a gain-of-function approach. cDNA encoding *Robo3* and its 3′UTR sequences (with a Myc-tag sequence) was cotransfected with HA-Msi1 into COS-7 cells. Western blot and RT-PCR analyses revealed that Myc-Robo3 protein, but not its mRNA, was clearly upregulated by HA-Msi1 in a dose-dependent manner (Figures 5D and 5E). Under this condition, an increased amount of *Robo3* mRNA was recruited to heavy polysomes, in which the mRNAs were actively translated, in Msi1-expressing cells (Figures S4C–S4E). These results suggest that Msi1 likely regulates Robo3 expression at the translational level.

We next examined the functional domains of Msi1 that are responsible for the regulation of Robo3 expression. Previous studies have indicated that Msi1 protein can be functionally divided into N- and C-terminal halves. The N-terminal half contains two RRMs (RNA recognition motifs), which are required for RNA binding, while the C-terminal half may have roles in interactions with other proteins (Kawahara et al., 2008). To assess the functions of the RRMs and the C-terminal half of Msi1 protein in the regulation of Robo3 expression, cDNAs encoding wild-type or the N-terminal half (ΔC) or the C-terminal half (ΔRRM) of Msi1 (Figure 6A) were cotransfected with cDNA encoding *Robo3* (including the 3′UTR) into COS-7 cells (Figures 6A–6C). While wild-type Msi1 increased the expression of Robo3 protein but not that of mRNA, ΔRRM failed to increase either the Robo3 protein or the mRNA (Figure 6B and 6C). On the other hand, ΔC still increased the expression of Robo3 protein, but not its mRNA, though to a lesser extent than the wild-type (Figures 6B and 6C). These results suggest that the RNA-binding of Msi1 is likely to be essential for the regulation of Robo3 expression. However, indirect binding of Msi1 to *Robo3* mRNA via RRMs cannot be excluded. The C-terminal half of Msi1 protein may also be required for a maximal effect, because ΔC was not as effective as the wild-type.

We next attempted to determine the region in *Robo3* mRNA that is responsible for Msi1-mediated regulation. Surprisingly, unlike previously identified target mRNAs, the 3′UTR of *Robo3* mRNA, which includes a single Msi1-binding consensus sequence, was not essential for Msi1-mediated regulation (Figures S5A–S5C). By expressing a series of deletion mutants of *Robo3* mRNA (Figure 6D) with Msi1 in COS-7 cells, we next tested the coding region of *Robo3* mRNA. Msi1 failed to increase the protein level of Myc-Robo3 CDS (coding sequence) 3208–4206 bp, while other deletion mutants of Myc-Robo3 were

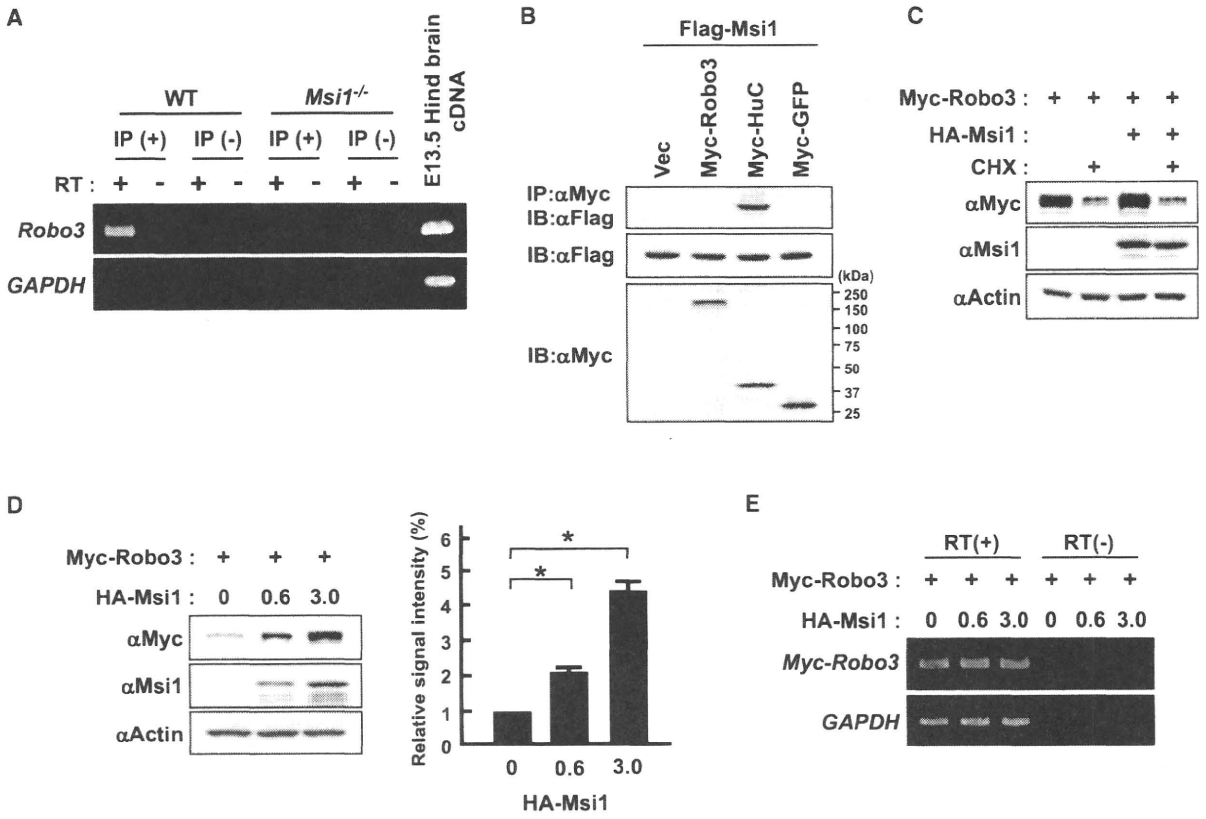

Figure 5. Msi1 Associates with *Robo3* mRNA, but Not Robo3 Protein, to Promote Expression

(A) In vivo RNA-protein binding assay combining affinity precipitation with RT-PCR. E13.5 hindbrain extracts were immunoprecipitated with anti-Msi1 antibody. RNA present in the precipitates was subjected to RT-PCR amplification using specific primers for *Robo3* and *GAPDH*. The right most lane indicates RT-PCR of RNA from E13.5 wild-type (WT) mouse hindbrain without immunoprecipitation.

(B) Immunoprecipitation assay for the interaction of Msi1 with Robo3 protein. Extracts of COS-7 cells transfected with the indicated expression vectors were immunoprecipitated (IP) with anti-Myc antibody and immunoblotted (IB) with anti-Flag antibody (top panel). Msi1 did not interact with Robo3 protein.

(C) Western blot analysis for the degradation of Robo3 protein. COS-7 cells were transfected with the optimized amounts of Myc-Robo3 and HA-Msi1, the conditions under which the upregulation of Robo3 by Msi1 (Figure 5D) was minimized, and cultured for 2 days. Then, the cells were treated with 10 μg/ml cycloheximide (CHX) for 20 hr.

(D) Western blot analysis. *Myc-Robo3* including its 3′UTR sequence and HA-Msi1 were coexpressed in COS-7 cells. The amount of the expression vector for HA-Msi1 is shown in micrograms per assay. The graph represents the relative signal intensities of Robo3 normalized to that of actin. The value obtained under the condition "HA-Msi1 0 μg" (leftmost lane) was set as 1. The data represent mean ± SEM of four independent experiments. The data were subjected to a repeated-measures ANOVA test, and p values were calculated by Bonferroni multiple comparison test: *$p < 0.001$.

(E) RT-PCR analysis under the same condition as described in (D).

(See also Figure S4.)

upregulated (Figure 6E), suggesting that the coding region harboring CDS 2059–3207 bp, which does not contain the Msi1-binding consensus sequence, is responsible for Msi1-mediated regulation. An RNA-protein binding assay using deletion mutants of *Robo3* mRNAs revealed that Msi1 binds to the *Robo3* coding sequence harboring only 2059–3222 bp sequence (Figures S5D and S5E). In agreement with these results, both Robo3.1 and Robo3.2, which are equally downregulated in *Msi1*$^{-/-}$ caudal hindbrain (Figures S3H–S3K), share the entire sequence of CDS 2059-3207 bp but only partially the 3′UTR (Chen et al., 2008). Taken together, these results suggest that, unlike other target mRNAs, Msi1 may regulate Robo3 expression through the coding region independently of the consensus binding sequence.

Msi1 Regulates Midline Crossing of Precerebellar Neurons by Controlling Robo3 Expression

The impaired midline crossing and the ipsilateral projection to the cerebellum of IO axons in *Msi1*$^{-/-}$ mice closely resemble the defects observed in *Robo3*$^{-/-}$ mice (Marillat et al., 2004). We further examined the architecture of the inferior olivary nucleus at P0 when IO neurons have assumed their final nuclear morphology (Figure 7A). In WT mice, the characteristic lamellar structures of the three subdivisions including the medial accessory olive (MAO), the dorsal accessory olive (DAO) and the principal olive (PO) were clearly observed on Nissl-stained sections (Figure 7Aa). However, in *Msi1*$^{-/-}$ and *Robo3*$^{-/-}$ mice, the morphologies of DAO and PO were apparently and quite similarly disorganized (Figures 7Aa and 7Ab). DAO were shortened and